

On the accuracy of HI observations in molecular clouds – More cold HI than thought?

D. Seifried,^{1*} H. Beuther,² S. Walch,¹ J. Syed,² J. D. Soler,² P. Girichidis,³ R. Wünsch⁴

¹Universität zu Köln, I. Physikalisches Institut, Zùlpicher Str. 77, 50937 Köln, Germany

²Max Planck Institute for Astronomy, Königstuhl 17, 69117 Heidelberg, Germany

³Universität Heidelberg, Zentrum für Astronomie, Institut für Theoretische Astrophysik, Albert-Ueberle-Str. 2, 69120 Heidelberg, Germany

⁴Astronomical Institute of the Czech Academy of Sciences, Bocni II 1401/1, 141 00 Prague 4, Czech Republic

Released 2021

ABSTRACT

We present a study of the cold atomic hydrogen (HI) content of molecular clouds simulated self-consistently within the SILCC-Zoom project for solar neighbourhood conditions. We produce synthetic observations of HI at 21 cm including HI self-absorption (HISA) and observational effects. We find that HI column densities, N_{HI} , of $\gtrsim 10^{22} \text{ cm}^{-2}$ are frequently reached in molecular clouds and that the HI gas reaches temperatures as low as $\sim 10 \text{ K}$. We show that HISA observations typically tend to underestimate the amount of cold HI in molecular clouds by a factor of 3 – 10 and produce an artificial upper limit of observed N_{HI} values around 10^{21} cm^{-2} . Based on this, we argue that the cold HI mass in molecular clouds could be a factor of a few higher than previously estimated. Also N_{HI} -PDFs obtained from HISA observations might be subject to observational biases and should be considered with caution. We demonstrate that the underestimation of cold HI in HISA observations is due to both the large HI temperature variations and the effect of noise in regions of high optical depth. In general, we find optical depths of cold HI around 1 – 10 making optical depth corrections essential. We show that the high HI column densities ($\gtrsim 10^{22} \text{ cm}^{-2}$) can in parts be attributed to the occurrence of up to 10 individual HI-H₂ transitions along the line of sight. However, also for a single HI-H₂ transition, N_{HI} frequently exceeds a value of 10^{21} cm^{-2} , thus challenging 1-dimensional, semi-analytical models. This can be attributed to non-equilibrium chemistry effects, which are included in our models, and the fact that HI-H₂ transition regions usually do not possess a 1-dimensional geometry. Finally, we show that the HI gas is moderately supersonic with Mach numbers of a few. The corresponding non-thermal velocity dispersion can be determined via HISA observations with an uncertainty of a factor of ~ 2 .

Key words: MHD – radiative transfer – methods: numerical – ISM: clouds – radio lines: ISM – ISM: atoms

1 INTRODUCTION

The chemical composition of molecular clouds (MCs) is still a field of active research. In particular the transition from atomic hydrogen (HI) to molecular hydrogen (H₂) is of interest. During the initial formation of MCs, HI is continuously transformed into H₂ as the cloud collapses and its density increases (e.g. Glover & Mac Low 2007b; Glover et al. 2010; Clark et al. 2012b; Mac Low & Glover 2012; Seifried et al. 2017, but see also the review by Dobbs et al. 2014). Knowledge about the exact content of HI and H₂ in MCs would also be of great value to assess the amount of CO-dark H₂ gas, i.e. molecular gas which is not traced by CO emission and thus affects the X_{CO} -factor (see e.g. the review by Bolatto et al. 2013).

Plenty of semi-analytical works studied the transition of HI- to H₂-dominated gas in MCs under various conditions with either plane-parallel or spherically symmetric models (e.g. van Dishoeck & Black 1986; Sternberg 1988; Röllig et al. 2007; Krumholz et al. 2008, 2009; Wolfire et al. 2010; Sternberg et al. 2014; Bialy & Sternberg 2016).

For solar-neighbourhood conditions these models predict that the HI-H₂ transition occurs around column densities of $\sim 10^{20} - 10^{21} \text{ cm}^{-2}$. Furthermore, beside the column density where the *transition* occurs, Sternberg et al. (2014) and Bialy & Sternberg (2016) also find that the *total* HI column density, N_{HI} , should be limited to a maximum of about 10^{21} cm^{-2} . These models are, however, typically highly idealised as they assume chemical equilibrium and are limited to a 1D geometry, although attempts are made to extend them to turbulent environments (Bialy et al. 2017b).

Modelling of the HI-H₂ transition in 3D, magneto-hydrodynamical (MHD) simulations remains a highly challenging task. This is due to that fact that MCs are not necessarily in chemical equilibrium concerning their hydrogen content due to turbulent mixing of H₂ into the lower-density environment (Glover et al. 2010; Valdivia et al. 2016; Seifried et al. 2017). Therefore, any simulation trying to study the physics and chemistry of the HI-H₂ transition in a self-consistent manner requires the inclusion of an on-the-fly chemical network. Moreover, in order to achieve a converged H₂ (and thus HI) content in the simulations, a high spatial resolution of $\sim 0.1 \text{ pc}$ is required (Seifried et al. 2017), which was confirmed subsequently by

* seifried@ph1.uni-koeln.de

means of semi-analytical considerations (Joshi et al. 2019). Despite these difficulties, there have been a great number of studies attempting to model the chemical composition of the (dense) interstellar medium (ISM) (e.g. Gnedin et al. 2009; Glover et al. 2010; Mac Low & Glover 2012; Valdivia et al. 2016; Bialy et al. 2017b; Clark et al. 2019; Joshi et al. 2019; Nickerson et al. 2019; Bellomi et al. 2020; Smith et al. 2020, and many more). However, not all of these studies fulfill the requirements of non-equilibrium chemistry and a sufficient spatial resolution. In agreement with semi-analytical results the HI-H₂ transition is found to occur around $\sim 10^{20} - 10^{21} \text{ cm}^{-2}$ (Gnedin et al. 2009; Valdivia et al. 2016; Seifried et al. 2017; Bellomi et al. 2020).

From the observational perspective, the HI content in the ISM is often determined via observations of the HI 21 cm emission line, UV absorption measurements and far-infrared studies. A large number of observations on both Galactic (e.g. Savage et al. 1977; Kalberla et al. 2005; Gillmon et al. 2006; Rachford et al. 2009; Barriault et al. 2010; Stanimirović et al. 2014; Lee et al. 2012, 2015; Burkhart et al. 2015; Imara & Burkhart 2016) and extragalactic scales (e.g. Wong & Blitz 2002; Browning et al. 2003; Blitz & Rosolowsky 2004, 2006; Bigiel et al. 2008; Wong et al. 2009; Schruba et al. 2011) find that the HI-H₂ transition occurs around $\sim 10^{20} - 10^{21} \text{ cm}^{-2}$. Furthermore, beside the value for the *transition*, some of these observations (e.g. Wong & Blitz 2002; Bigiel et al. 2008; Barriault et al. 2010; Schruba et al. 2011; Lee et al. 2012; Stanimirović et al. 2014; Burkhart et al. 2015) also suggest an upper *threshold* of N_{HI} around 10^{21} cm^{-2} , similar to the aforementioned semi-analytical models.

On smaller scales of individual MCs, the measurement of their cold HI content via the HI 21 cm line is challenging due to the simultaneous emission of HI in the warm neutral medium. This problem can be overcome by the study of HI self-absorption (HISA) first reported by Heeschen (1954, 1955). These HISA features arise when cold HI in the foreground absorbs the emission of warmer HI in the background (e.g. Knapp 1974). Over the last decades there have been numerous HISA observations studying the properties of HI gas in MCs (e.g. Riegel & Crutcher 1972; Knapp 1974; van der Werf et al. 1988; Goodman & Heiles 1994; Montgomery et al. 1995; Gibson et al. 2000, 2005; Kavars et al. 2003, 2005; Li & Goldsmith 2003; Goldsmith & Li 2005; Klaassen et al. 2005; Krčo et al. 2008; Krčo & Goldsmith 2010; Dénes et al. 2018; Beuther et al. 2020; Syed et al. 2020; Wang et al. 2020b). Similar to the observations on galactic scales and semi-analytical models, a large number of these HISA observations towards MCs seem to confirm an upper column density threshold of a few 10^{21} cm^{-2} for cold HI. However, there have been observations which report partly significantly higher HI column densities up to $\sim 10^{22} \text{ cm}^{-2}$ (Fukui et al. 2014, 2015; Motte et al. 2014; Bihr et al. 2015; Okamoto et al. 2017; Dénes et al. 2018). These observations thus challenge the picture of a saturation of N_{HI} around 10^{21} cm^{-2} obtained from other observational works and semi-analytical methods.

It is therefore necessary to assess the accuracy of HISA observations towards MCs in a fully self-consistent manner. Some of the first synthetic HI observations are presented by Douglas et al. (2010) and Acreman et al. (2010, 2012), modelling the HI emission on galactic scales with resolutions around a few 1 pc, i.e. stemming from the more diffuse, atomic ISM. On similar scales, Kim et al. (2014), and in associated follow-up studies Murray et al. (2015, 2017), conclude that HI absorption observations can trace parameters like the N_{HI} and the spin temperature with an accuracy of a few 10%. However, the authors do not include a chemical network for HI-H₂ and only apply a simplified radiative transfer method without observational effects such as noise or beam smearing. On smaller scales of indi-

vidual MCs, both Hennebelle et al. (2007) and Heiner et al. (2015) present HI spectra from simulations without any chemical network and only a simplified radiative transfer method. However, on these scales HI and H₂ coexist and are out of equilibrium due to turbulent mixing (Glover & Mac Low 2007b; Valdivia et al. 2016; Seifried et al. 2017) and thus the predictive power of these studies is limited. Fukui et al. (2018) present synthetic HI spectra of colliding flow simulations including a chemical network for HI and H₂. The authors find that for a significant portion of the pixels, N_{HI} can be underestimated in a non-negligible manner by several 10% and more, in particular in pixels with high optical depths. They do, however, not report any HI self-absorption features nor include observational effects. Furthermore, as the authors consider a MC at an extremely early evolutionary stage, their findings rather apply to the cold and warm neutral medium. Finally, Soler (2019) apply the method of oriented gradients to synthetic HISA observations of MCs modelled by Clark et al. (2019).

Following these works, here we present fully self-consistent synthetic HISA observations of MCs, that is, including 3D, MHD simulations with a chemical network, high spatial resolution ($\sim 0.1 \text{ pc}$), self-consistent radiative calculations and observational effects. We investigate the accuracy of HISA observations towards MCs (Section 3) and discuss implications of our findings for the postulated saturation of N_{HI} around 10^{21} cm^{-2} (Section 4). In particular we show that this saturation of N_{HI} could be a purely observational effect and/or a consequence of oversimplifying assumptions in semi-analytical models (Section 5). We conclude our work in Section 6.

2 NUMERICS

2.1 Simulations

We here briefly describe the numerics behind the simulations, for more details we refer to Seifried et al. (2017, 2019). All simulations are performed with the FLASH code (Fryxell et al. 2000; Dubey et al. 2008). We include a chemical network for H₂, H, H⁺, C⁺, C, O, CH, OH, CO, HCO⁺, He, He⁺, M and M⁺ (Nelson & Langer 1999; Glover & Mac Low 2007a,b; Glover & Clark 2012) with updates in the network described in Mackey et al. (2019). Here, M and M⁺ represent the contribution of metals, where we specifically consider Si and its first ionised state. We also include the most relevant heating and cooling mechanisms. In addition, we calculate the attenuation of the interstellar radiation field ($G_0 = 1.7$ in Habing units, Habing 1968; Draine 1978) using the TREE-RAY/OPTICAL-DEPTH module (Clark et al. 2012a; Walch et al. 2015; Wünsch et al. 2018). The cosmic ray ionisation rate of atomic hydrogen is set to $3 \times 10^{-17} \text{ s}^{-1}$. The Poisson equation for self-gravity is solved using a tree-based method (Wünsch et al. 2018).

The simulations are part of the SILCC-Zoom project (Seifried et al. 2017, 2020a), where we model the formation and evolution of MCs located in a part of a stratified galactic disk, which in turn is part of the SILCC project (Walch et al. 2015; Girichidis et al. 2016). The disk has an initial Gaussian density profile given by

$$\rho(z) = \rho_0 \times \exp \left[-\frac{1}{2} \left(\frac{z}{h_z} \right)^2 \right], \quad (1)$$

with $h_z = 30 \text{ pc}$ and $\rho_0 = 9 \times 10^{-24} \text{ g cm}^{-3}$, resulting in a total gas surface density of $\Sigma_{\text{gas}} = 10 \text{ M}_{\odot} \text{ pc}^{-2}$. We run two simulations, one without a magnetic field and one with. For the magnetized run we initialise the magnetic field as

$$B_x = B_{x,0} \sqrt{\rho(z)/\rho_0}, \quad B_y = 0, \quad B_z = 0, \quad (2)$$

with $B_{x,0} = 3 \mu\text{G}$ in accordance with observations (Beck & Wielebinski 2013). We emphasise that the magnetic field is dynamically important for the (chemical) evolution of the MCs (Seifried et al. 2020a,b). In addition to the gas self-gravity we include a background potential from the old stellar component modelled as an isothermal sheet with a scale height of 100 pc and $\Sigma_{\text{star}} = 30 \text{ M}_{\odot} \text{ pc}^{-2}$.

In the initial simulation phase, up to a time t_0 , the spatial resolution is 4 pc and we drive turbulence by injecting supernovae (SNe) with a rate of 15 SNe Myr^{-1} (see Walch et al. 2015; Girichidis et al. 2016; Gatto et al. 2017, for details). At t_0 we stop the SN injection to allow for the formation of MCs unaffected by nearby SN remnants, which could influence their evolution (Seifried et al. 2018). For both the unmagnetized and the magnetized run, we pick two regions, each with a typical size of $\sim (100 \text{ pc})^3$, in which MCs are about to form. We thus have in total 4 MCs, henceforth denoted as MC1-HD, MC2-HD, MC3-MHD and MC4-MHD, where the first two are non-magnetised runs and the latter two include a dynamically relevant magnetic field (as in Seifried et al. 2020a, where we discuss their chemical properties concerning H_2 and CO). The typical H_2 masses of these clouds are around $20 - 50 \times 10^3 \text{ M}_{\odot}$, and for the magnetized runs the volume-weighted magnetic field is around $4 \mu\text{G}$. Starting at t_0 , we then progressively increase the spatial resolution in these zoom-in regions over 1.65 Myr reaching a maximum resolution of 0.06 pc. Afterwards, we evolve the clouds on this resolution for a few more Myr. We note that throughout the paper all times refer to the time elapsed since t_0 , i.e. the start of the zoom-in procedure. We have $t_0 = 11.9$ and 16.0 Myr for the runs without and with magnetic fields, respectively.

2.2 Radiative transfer

The radiative transfer simulations are performed in a post-processing step with RADMC-3D (Dullemond et al. 2012) for the HI 21 cm emission line of atomic hydrogen. In order to calculate the (two-) level population, we apply the method to calculate the spin temperature of atomic hydrogen, T_s , described in Kim et al. (2014, their Eqs. 4 – 7). In particular, we include the Wouthuysen-Field (WF) effect (Wouthuysen 1952; Field 1958) assuming $T_{\alpha} = T_{\text{gas}}$ for the effective temperature of the $\text{Ly}\alpha$ field (Field 1959) and $n_{\alpha} = 10^6 \text{ cm}^{-3}$ for the $\text{Ly}\alpha$ photon density (Liszt 2001). We emphasise that including or excluding the WF effect has only a marginal impact as for the temperatures of $\lesssim 10^2 \text{ K}$ typical for MCs, the WF effect does barely affect T_s , which remains close to the actual gas temperature in both cases (fig. 2 of Kim et al. 2014). Furthermore, the Einstein coefficient of the HI line is $A_{ul} = 2.8843 \times 10^{-15} \text{ s}^{-1}$ (Gould 1994) and the spectral resolution is set to 200 m s^{-1} over a range of $\pm 20 \text{ km s}^{-1}$ resulting in 201 velocity channels.

We consider the emission of the four MCs in isolation, i.e. the emission stemming from the gas in the aforementioned zoom-in regions only. This allows us to focus on the HISA signal originating from the MCs themselves (and to a smaller extent from warm HI in the zoom-in region) avoiding any foreground contamination. We use a resolution of 0.06 pc, i.e. identical to the maximum resolution of the underlying simulations. We investigate the emission for two points in time, that is $t_{\text{evol}} = 2$ and 3 Myr . As the results for both times are qualitatively similar, for most of the plots we focus on $t_{\text{evol}} = 2 \text{ Myr}$. In order to model the emission (and its absorption) of a diffuse HI background, we include a fixed background radiation field with a radiation temperature of 100 K in the radiative transfer calculation. This background temperature is motivated by results from recent HISA observations (Syed et al. 2020; Wang et al. 2020b) and is also

used in the numerical study presented in Soler et al. (2019). This makes our HISA observations sensitive to absorption of HI gas with T_s below 100 K, warmer gas will be seen in emission. We note that we have also tested the usage of a background temperature of 200 K. The observed changes are, however, only very moderate which is why we focus on the case of 100 K here.

2.2.1 Adding observational effects

In a final step we incorporate observational effects into our obtained (ideal) HI emission maps. For this purpose we (i) convolve our emission maps with a Gaussian beam of $80''$ (at the chosen distance, see below), (ii) reduce the spectral resolution from 200 m s^{-1} to 1 km s^{-1} by summing up the contribution of 5 neighbouring channels and (iii) finally add random Gaussian noise with a standard deviation of 3 K to the obtained emission maps¹. All the above stated values are average values from recent HISA observations towards MCs (e.g. Dénes et al. 2018; Beuther et al. 2020; Syed et al. 2020; Wang et al. 2020b). We choose two different distances for the observed clouds of 150 pc and 3 kpc, corresponding to a physical beam size of 0.06 pc and 1.2 pc, respectively. However, as the results for both distances are relatively similar, in the following we focus on the distance of 150 pc.

2.3 HISA calculations

In order to investigate the properties of the absorbing atomic hydrogen gas, i.e. the HISA features, we follow the approach described in Wang et al. (2020b, see their section 2.2) to convert the absorption spectrum into an effective emission spectrum of the cold HI. In short, assuming that both foreground and background emission are optically thin, one can relate the observed emission to the temperature, T_{HISA} , and optical depth, τ_{HISA} , of the absorbing, cold HI gas via

$$T_{\text{off-on}} = T_{\text{off}} - T_{\text{on}} = (pT_{\text{off}} + T_{\text{cont}} - T_{\text{HISA}}) \times (1 - e^{-\tau_{\text{HISA}}}). \quad (3)$$

For the sake of readability, we have omitted the dependence on the velocity channel in the above equation. Here, T_{on} is the actually observed brightness temperature, and T_{off} is the brightness temperature at an off-position, i.e. the radiation temperature which would be measured if no absorbing cold HI gas were present along the line of sight (LOS) towards the observer. Furthermore, T_{cont} is the brightness temperature of the diffuse continuum background, and the dimensionless quantity p parametrises the ratio of foreground to background emission (Feldt 1993; Gibson et al. 2000) and is usually estimated to be close to 1 (McClure-Griffiths et al. 2006; Rebolledo et al. 2017; Dénes et al. 2018; Wang et al. 2020b).

In Wang et al. (2020b), T_{off} – which is not accessible via observations – is inferred by fitting a polynomial to the absorption-free channels, i.e. those channels where no HISA feature is present. As in our synthetic observations we use a fixed background radiation temperature of 100 K, the spectrum in the absorption-free channels is practically flat as the emission of HI gas warmer than 100 K in the considered zoom-in region is almost negligible, similar to the findings of Soler et al. (2019). For this reason, we can set $T_{\text{off}} = 100 \text{ K}$ for our data which yields

$$T_{\text{off-on}}(v) = 100 \text{ K} - T_{\text{on}}(v). \quad (4)$$

¹ Note that it is important to apply step (iii) as the final step.

The quantity $T_{\text{off-on}}(\nu)$ is positive and gives the depth of the absorption feature seen in $T_{\text{on}}(\nu)$. In the following we refer to these kind of spectra as HISA spectra.

Furthermore, using a constant background temperature and assuming that the emission of HI warmer than 100 K is negligible is congruent with setting $p = 1$ and $pT_{\text{off}} + T_{\text{cont}} = 100 \text{ K}$ ². Hence, we can simplify Eq. 3 to yield

$$T_{\text{off-on}}(\nu) = (100 \text{ K} - T_{\text{HISA}}) \times (1 - e^{-\tau_{\text{HISA}}(\nu)}). \quad (5)$$

We apply the spectral analysis tool BTS³ (Clarke et al. 2018) to $T_{\text{off-on}}(\nu)$ to find the location and properties of the HISA feature. BTS identifies and fits Gaussian peaks in a spectrum. Assuming that the HISA feature has approximately the shape of a single Gaussian, we restrict the fitting function used in BTS to a single Gaussian. We set the noise level to 3 K and the required signal-to-noise ratio to 3. Of the obtained fitting values, here only the line width, σ_{BTS} , will be used later in the paper. Next, for each pixel for which BTS identifies a (Gaussian) HISA feature, we calculate the column density of the cold HI responsible for the HISA feature.

For this purpose, for most of our paper we adopt a fixed value for T_{HISA} for the entire map, identical to the approach applied in recent observations (e.g. Syed et al. 2020; Wang et al. 2020b, but see below and Section 3.5 for a different approach). We then solve Eq. 5 for the optical depth of the HISA feature, τ_{HISA} , for each channel independently, which yields

$$\tau_{\text{HISA}}(\nu) = -\ln \left(1 - \frac{T_{\text{off-on}}}{100 \text{ K} - T_{\text{HISA}}} \right). \quad (6)$$

With this we can calculate the column density of the HISA feature via (Wilson et al. 2013)

$$N_{\text{HI,obs}} = 1.8224 \times 10^{18} \text{ cm}^{-2} \frac{T_s}{1 \text{ K}} \int \tau(\nu) \frac{d\nu}{1 \text{ km s}^{-1}}, \quad (7)$$

where we assume $T_s = T_{\text{HISA}}$ for the HI spin temperature and $\tau(\nu) = \tau_{\text{HISA}}(\nu)$ for the optical depth.

Though being straightforward to use, this method has the disadvantage that a fixed value of T_{HISA} for every pixel of the map has to be assumed, which might not be the case. Furthermore, when choosing a fixed T_{HISA} , Eq. 3 might not yield a result for τ_{HISA} for every channel. The maximum useable value for each channel, $T_{\text{HISA,max}}(\nu)$, is obtained by assuming $\tau_{\text{HISA}} \rightarrow \infty$ (Wang et al. 2020b), which results for our setup in

$$T_{\text{HISA,max}}(\nu) = -T_{\text{off-on}}(\nu) + pT_{\text{off}}(\nu) + T_{\text{cont}} = T_{\text{on}}(\nu). \quad (8)$$

Hence, if the assumed T_{HISA} exceeds the observed radiation temperature $T_{\text{on}}(\nu)$ of a given channel, this channel has to be dropped and cannot be taken into account for the calculation of the column density (see Section 3.2).

An alternative way to determine the optical depth, which simultaneously leaves T_{HISA} as a free parameter, is given by Knapp (1974) expressing $\tau_{\text{HISA}}(\nu)$ via

$$\tau_{\text{HISA}}(\nu) = \tau_0 e^{-\frac{1}{2} \left(\frac{\nu - \nu_0}{\sigma_0} \right)^2}. \quad (9)$$

Here, τ_0 , ν_0 and σ_0 are free parameters (together with T_{HISA}) which are determined by fitting the observed spectrum $T_{\text{off-on}}(\nu)$ with Eq. 9 inserted in Eq. 5. As before, the fit is only performed for those pixels where we identify a Gaussian HISA feature with BTS. Beside the

² Effectively, we now do not differentiate any more between pT_{off} and T_{cont} .

³ Acronym for “Behind The Spectrum”, <https://github.com/SeamusClarke/BTS>

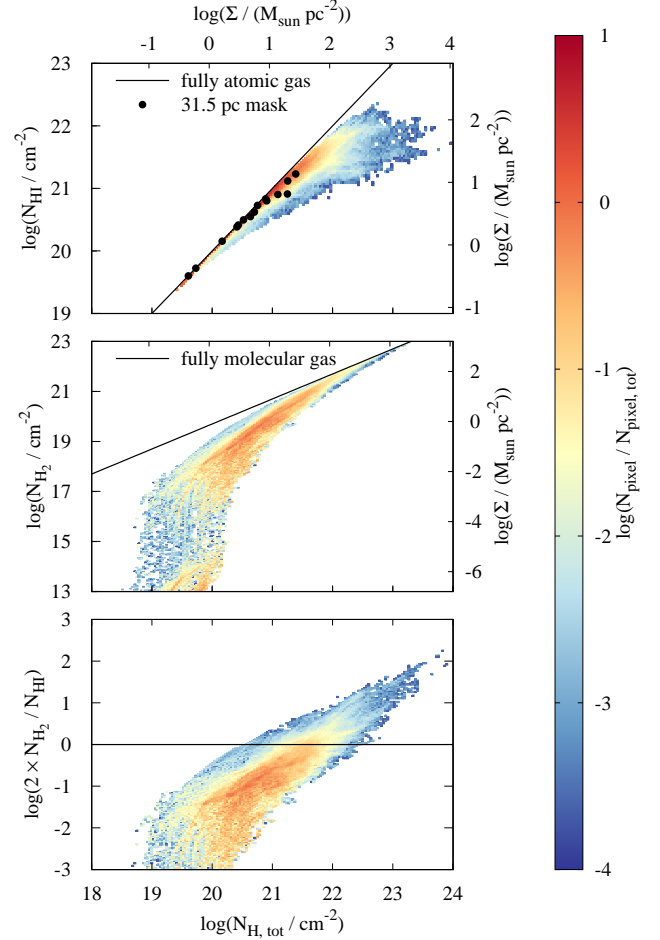


Figure 1. 2D-PDF of N_{HI} (top) and N_{H_2} (middle) and ratio of both column densities vs. $N_{\text{H,tot}}$ (bottom) for MC1-HD at 3 Myr for one LOS. The HI-H₂ transition occurs around 10^{21} cm^{-2} in rough agreement with observational results. However, the HI column density levels off only around a few 10^{22} cm^{-2} , thus higher than typically obtained in observations. Black dots denote the average column density when using pixels with a size of $(31.5 \text{ pc})^2$ (see Section 5). Note the different y-axis scaling for the top and middle panel.

approach using a fixed T_{HISA} we will also test this approach in the following.

3 RESULTS

In order to get a first impression about the HI and H₂ content of the simulated MCs, in Fig. 1 we show the 2D-PDFs of N_{H_2} , N_{HI} and their ratio vs. $N_{\text{H,tot}}$ for a selected simulation snapshot. Here, $N_{\text{H,tot}} = N_{\text{HI}} + 2 N_{\text{H}_2} + N_{\text{H}^+}$ denotes the total hydrogen column density. We find that H₂ starts to form above $N_{\text{H,tot}} \approx 10^{20} \text{ cm}^{-2}$. The transition from atomic- to molecular-hydrogen dominated gas, however, occurs around $N_{\text{H,tot}} \approx 10^{21} \text{ cm}^{-2}$ ($\approx 8 M_{\odot} \text{ pc}^{-2}$), as discussed in detailed in Seifried et al. (2020a). This is in agreement with other numerical and semi-analytical works (Krumholz et al. 2008, 2009; Gnedin et al. 2009; Sternberg et al. 2014; Bialy & Sternberg 2016; Valdivia et al. 2016; Bellomi et al. 2020).

However, despite H₂ forming rapidly above $N_{\text{H,tot}} \approx 10^{20} \text{ cm}^{-2}$, also N_{HI} continues to rise. Most of the HI has column densities around 10^{21} cm^{-2} ($\approx 8 M_{\odot} \text{ pc}^{-2}$) similar to theoretical predictions

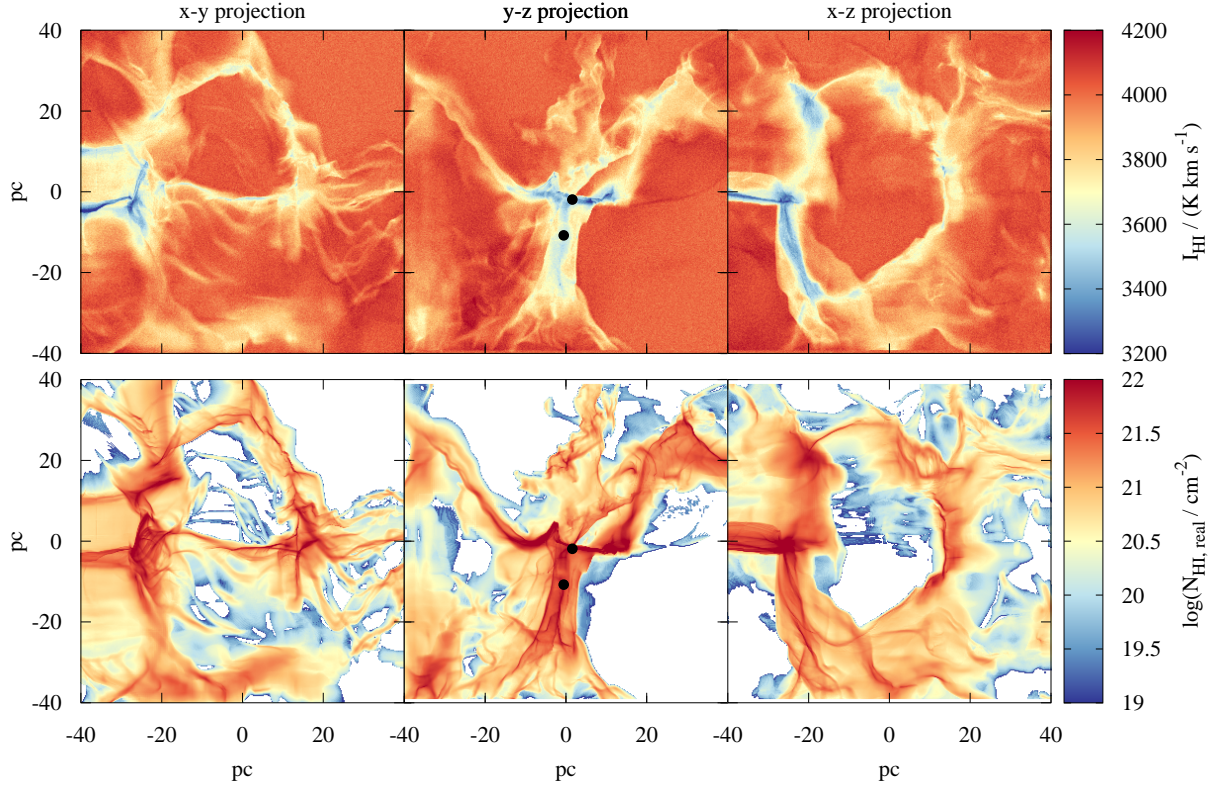


Figure 2. Top row: Integrated HI intensity for three different directions of MC1-HD at $t_{\text{evol}} = 2$ Myr including observational effects for an assumed distance of 150 pc (beam size corresponds to 0.06 pc). Bottom row: Column density of HI gas with temperatures below 100 K calculated directly from the simulation data. The HISA feature traces well the high-column density regions. Note that the high integrated intensities around 4000 K km s⁻¹ are due to the assumed constant background radiation temperature of 100 K integrated over a velocity range of ± 20 km s⁻¹. The black dots in the middle column show the positions of the two LOS for which the spectra are plotted in Fig. 3.

(Krumholz et al. 2008, 2009; Sternberg et al. 2014; Bialy & Sternberg 2016). However, even significantly higher HI column densities up to a few 10^{22} cm⁻² are reached, i.e. H₂ and HI coexist on the projected maps. Hence, having the HI-H₂ transition around a certain value (e.g. 10^{21} cm⁻²) does *not* exclude the occurrence of significantly higher HI column densities.

3.1 Deriving N_{HI} using a fixed T_{HISA}

In the following we will assess how accurately the *cold* HI content in MCs can be determined via HISA observations⁴. We define cold HI as all HI with temperatures below 100 K. This definition is motivated by the chosen background radiation temperature (Section 2.3), which makes our synthetic HISA observations sensitive to HI with temperatures below 100 K. Depending on the simulation, we find that around and in our MCs 22 – 47% of the HI is warmer than 100 K, i.e. in all cases the HISA observations are sensitive to more than 50% of the entire HI mass. In the top row of Fig. 2, we show the velocity-integrated intensity, I_{HI} , of our synthetic HI observations of MC1-HD from three different directions at $t_{\text{evol}} = 2$ Myr including observational effects at an assumed distance of 150 pc (see Section 2.2.1). For $t_{\text{evol}} = 3$ Myr the results are qualitatively similar. In

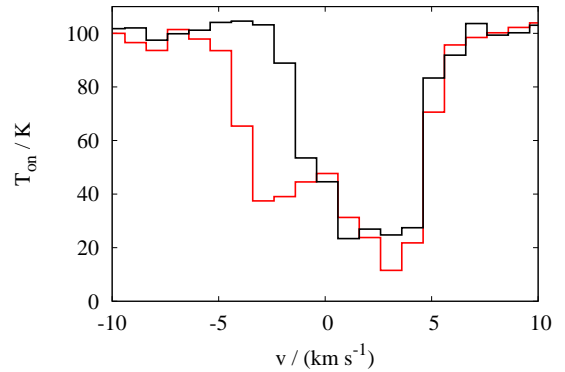


Figure 3. Synthetic HI spectra including observational effects for two LOS in the map shown in the top middle panel of Fig. 2 (black dots). The black line shows a spectrum potentially suffering from opacity broadening at the line center. In the spectrum shown by the red line two absorption features around $v = \pm 3$ km s⁻¹ seem to be present.

the bottom row we show the cold HI column density of MC1-HD inferred directly from the simulation, $N_{\text{HI,real}}$. We emphasise that throughout this paper $N_{\text{HI,real}}$ refers to the cold HI gas ($T \leq 100$ K) as described above.

Both the synthetic HI emission and the $N_{\text{HI,real}}$ -maps show complex filamentary structures with extended envelopes. There is a clear

⁴ In Seifried et al. (2020a) we have already discussed a new approach to determine the H₂ content by means of combined CO(1-0) and dust emission observations, which allows for an accurate determination of H₂ within a factor of 1.8.

anti-correlation between I_{HI} and $N_{\text{HI,real}}$ visible. In order to demonstrate that the drop in I_{HI} is due to the self-absorption of radiation, we show in Fig. 3 two example spectra from pixels in the high- $N_{\text{HI,real}}$ /low- I_{HI} areas in the middle column of Fig. 2 (black dots). For both pixels there are clear HISA features recognisable caused by the cold HI. For the other MCs and an assumed distance of 3 kpc, the obtained results are qualitatively and quantitatively very similar. We note that the rather high integrated intensities around 4000 K km s^{-1} are due to the assumed constant background radiation temperature of 100 K integrated over a velocity range of $\pm 20 \text{ km s}^{-1}$, which is, however, automatically taken into account via Eq. 5.

Next, we investigate the HI column densities obtained from the HISA observations, denoted as $N_{\text{HI,obs}}$ (Eq. 7), assuming a fixed HISA temperature, T_{HISA} . In the top row of Fig. 4 we show $N_{\text{HI,obs}}$ for $T_{\text{HISA}} = 20, 40$ and 60 K for MC1-HD at $t_{\text{evol}} = 2 \text{ Myr}$ for one LOS at an assumed distance of 150 pc . In the bottom row we show the ratio of $N_{\text{HI,obs}}$ and $N_{\text{HI,real}}$. Most prominently, we find that for all three values of T_{HISA} , the observed column densities $N_{\text{HI,obs}}$ in the central and most dense regions are a factor of ≥ 10 too low. This trend becomes more pronounced with increasing T_{HISA} . In the outer regions $N_{\text{HI,obs}}$ could not be calculated for all pixels as here the absorption features are partly too weak and therefore the spectral analysis tool BTS does not identify any HISA feature. For the remaining pixels in the outer parts, $N_{\text{HI,real}}$ is also typically underestimated ranging from a few 10% up to a factor of a few. However, increasing T_{HISA} pushes $N_{\text{HI,obs}}$ in the outer regions closer to $N_{\text{HI,real}}$. Overall, however, the match between the actual and observed HI column density is rather poor with a clear tendency to underestimate $N_{\text{HI,real}}$ by factors up to ~ 10 (see also Section 3.4 for the effect on total estimated HI mass). This does not change when considering different LOS, times, MCs or assuming a distance of 3 kpc. Reasons for this underestimation will be discussed in detail in Sections 3.2 and 3.3.

In Fig. 5 we show the mean value of $N_{\text{HI,obs}}$ as a function of $N_{\text{HI,real}}$ for the four different MCs placed at 150 pc at $t_{\text{evol}} = 2 \text{ Myr}$ focussing on the case of $T_{\text{HISA}} = 20, 40$ and 60 K (coloured lines). Overall, the underestimation shown in Fig. 4 is observed in all cases, the degree of underestimation becomes more pronounced with increasing $N_{\text{HI,real}}$ and decreasing T_{HISA} . Lowering or increasing T_{HISA} beyond the values shown only amplifies the trends, which is why we do not explicitly discuss them here. In the following we focus on the range of $N_{\text{HI,real}} \geq 10^{19.5} \text{ cm}^{-2}$.

First, we note that $T_{\text{HISA}} = 20 \text{ K}$ (blue lines) is apparently a rather bad choice resulting in an underestimation by about one order of magnitude (and more). Considering $T_{\text{HISA}} = 60 \text{ K}$ (red lines), we find that in the range $10^{19.5} \text{ cm}^{-2} \lesssim N_{\text{HI,real}} \lesssim 10^{21} \text{ cm}^{-2}$, the actual values are underestimated by a factor of $\sim 2 - 5$. In the same range, for $T_{\text{HISA}} = 40 \text{ K}$ (green lines), the actual values are underestimated even more severely by a factor of $\sim 3 - 10$. Moreover, for $N_{\text{HI,real}} > 10^{21} \text{ cm}^{-2}$, $N_{\text{HI,obs}}$ seems to level off around $\sim 10^{20.5-21} \text{ cm}^{-2}$, for both $T_{\text{HISA}} = 40$ and 60 K . This results in an increasing underestimation of the actual column density when going to denser and denser regions. We note that this artificial leveling-off around $N_{\text{HI,obs}} \approx 10^{21} \text{ cm}^{-2}$ matches well the maximum values reported in recent HISA observations (Kavars et al. 2003, 2005; Li & Goldsmith 2003; Goldsmith & Li 2005; Klaassen et al. 2005; Krčo et al. 2008; Barriault et al. 2010; Krčo & Goldsmith 2010; Syed et al. 2020; Wang et al. 2020b, but see also Section 4.1 for a further discussion). Finally, even for a single MC there is a large scatter of the measured $N_{\text{HI,obs}}$ for a given $N_{\text{HI,real}}$ (shown by the full distribution in grey scale in the background for MC1-HD for $T_{\text{HISA}} = 40 \text{ K}$). This further lowers the accuracy with which HISA observations seem to be able to constrain the actual HI column density.

Table 1. List of the most relevant temperature definitions used in this paper including a short explanation

T_{HISA}	assumed temperature of the HISA features needed for the calculation of the HI optical depth (Eq. 6) and subsequently the column density
$T_{\text{HI,mw}}$	mass-weighted HI temperature calculated from the simulation data for a given pixel, see right panel of Fig. 6
$T_{\text{on}}(v)$	spectrum of the measured HI radiation temperature for a given pixel, see Fig. 3
T_{dip}	lowest temperature of the T_{on} spectrum for a given pixel, see Eq. 10 and left panel of Fig. 6

3.2 The HI temperature

Investigating Eq. 3 shows that there is a certain upper threshold for T_{HISA} , up to which a result for τ_{HISA} can be achieved for every velocity channel. Setting T_{HISA} above this value would render the equation unsolvable for τ_{HISA} for at least some of the velocity channels, which in consequence would have to be omitted for the calculation of N_{HI} . We denote this upper threshold as T_{dip} , which is set by the minimum of $T_{\text{HISA,max}}(v)$ (Eq. 8) over all velocity channels for a given pixel, i.e.

$$T_{\text{dip}} = \min(T_{\text{HISA,max}}(v)) = \min(T_{\text{on}}(v)). \quad (10)$$

The denomination as T_{dip} is motivated by the fact that it corresponds to the temperature at the dip of the observed absorption spectrum $T_{\text{on}}(v)$. It can also be considered as a proxy for the actual temperature of the HISA feature. In Table 1 we give a short summary of the most relevant temperature definitions used in this paper.

In the left panel of Fig. 6 we show the map of T_{dip} for one snapshot. In addition, the right panel shows the actual mass-weighted, LOS-averaged HI temperature, $T_{\text{HI,mw}}$ ⁵. Both T_{dip} and $T_{\text{HI,mw}}$ show a strong drop towards the central, high-column density areas (see also top panel of Fig. 7). Interestingly, we find that both temperature measures show an agreement typically within about 20 K , and we suggest that T_{dip} can be used as an approximate probe of the temperature of the cold HI along the LOS.

The strong variations, in particular the drop of T_{dip} down to values as low as $\sim 10 \text{ K}$, can explain the significant underestimation of $N_{\text{HI,real}}$ seen in the Figs. 4 and 5, which we attribute to two effects explained in the following and which are sketched in Fig. 7:

(i) $T_{\text{HISA}} > T_{\text{dip}}$: These regions typically correspond to high $N_{\text{HI,real}}$ ($\gtrsim 10^{21} \text{ cm}^{-2}$) (top panel of Fig. 7). Here, Eq. 3 does not yield any results for at least some of the velocity channels. This happens for $\lesssim 10\%$, $5 - 20\%$, and $30 - 40\%$ of the pixels for $T_{\text{HISA}} = 20, 40$, and 60 K , respectively. Hence, for these pixels some of the channels have to be neglected, which reduces $N_{\text{HI,obs}}$ significantly (Eq. 7). As with decreasing T_{dip} , i.e. increasing $N_{\text{HI,real}}$, more and more velocity channels have to be omitted (at a fixed T_{HISA}), this leads to the observed artificial levelling-off of $N_{\text{HI,obs}}$ at $\sim 10^{21} \text{ cm}^{-2}$. In consequence, for central, high column density regions of MCs, $N_{\text{HI,real}}$ is underestimated by a factor of about 10 and more (Fig. 5).

(ii) $T_{\text{HISA}} < T_{\text{dip}}$: If T_{HISA} is chosen too low, also the derived optical depth τ_{HISA} is underestimated (Eq. 6). As $N_{\text{HI,obs}}$ depends

⁵ As the synthetic HI observations are only sensitive to HI with temperatures below 100 K , also for this average (as for $N_{\text{HI,real}}$) only HI gas with $T \leq 100 \text{ K}$ is considered.

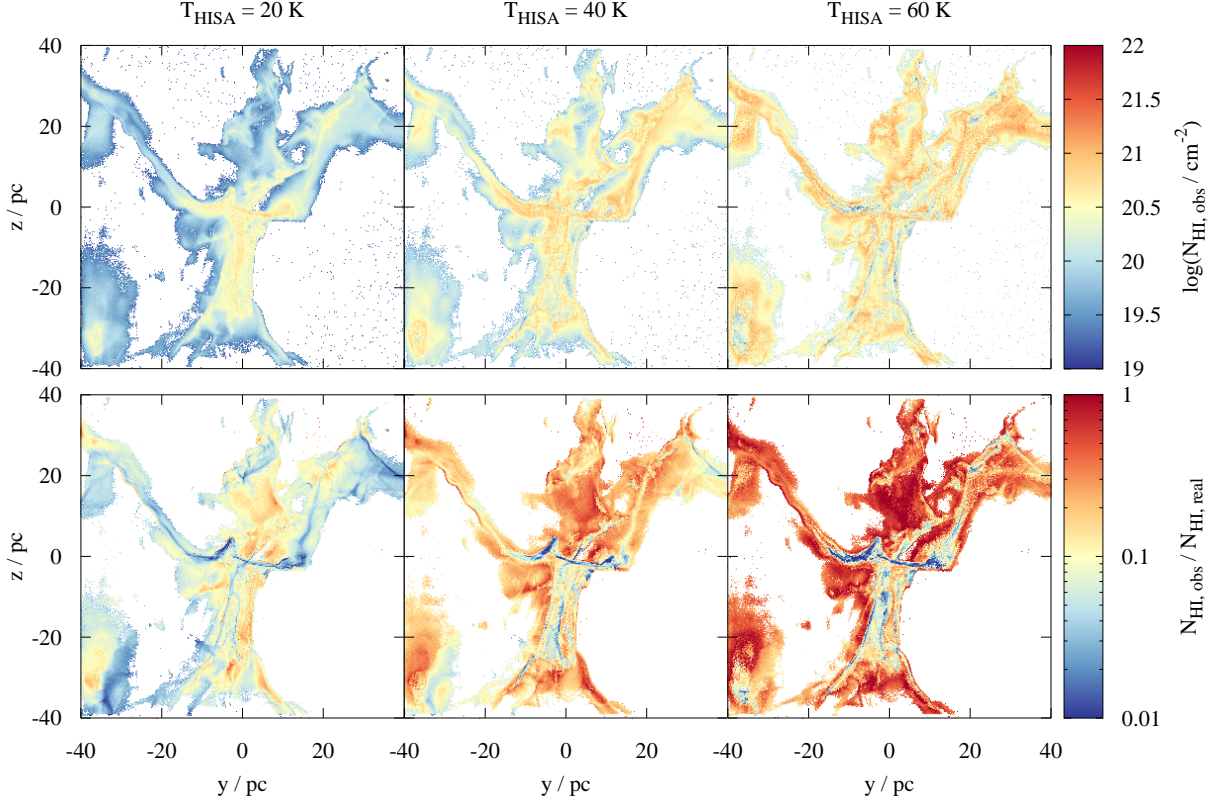


Figure 4. Top row: Observed HI column density assuming a fixed T_{HISA} of 20, 40 and 60 K (from left to right) for MC1-HD at $t_{\text{evol}} = 2$ Myr at an assumed distance of 150 pc (beam size corresponds to 0.06 pc). Bottom row: Ratio of the observed HI column density shown in the top row to the actual HI column density (for $T < 100$ K). Overall, assuming a fixed T_{HISA} underestimates $N_{\text{HI,real}}$ by almost about one order of magnitude in the central, high column density regions. Increasing T_{HISA} improves the match only in the outer regions.

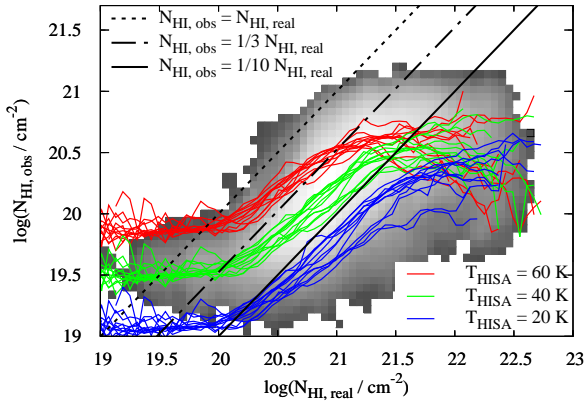


Figure 5. Mean value of $N_{\text{HI,obs}}$ against $N_{\text{HI,real}}$ for the three different directions of all four MCs placed at a distance of 150 pc at $t_{\text{evol}} = 2$ Myr and using three different T_{HISA} (colored lines). In the background the full distribution for one snapshot (MC1-HD, $T_{\text{HISA}} = 40$ K) is shown in grey scale. The black lines show lines of constant ratio $N_{\text{HI,obs}}/N_{\text{HI,real}}$ to guide the readers eye. In general, the actual column density is underestimated significantly, and the maximum $N_{\text{HI,obs}}$ levels off around 10^{21} cm^{-2} .

linearly on both T_{HISA} and τ_{HISA} (Eq. 7), this also results in an underestimation of $N_{\text{HI,real}}$. This effect is dominant mainly in the low to intermediate column density regions in the outer parts of the MCs ($N_{\text{HI,real}} \leq 10^{21} \text{ cm}^{-2}$). Here, $N_{\text{HI,obs}}$ underestimates $N_{\text{HI,real}}$ on average by a factor of 3 – 10. Due to the linear dependence of

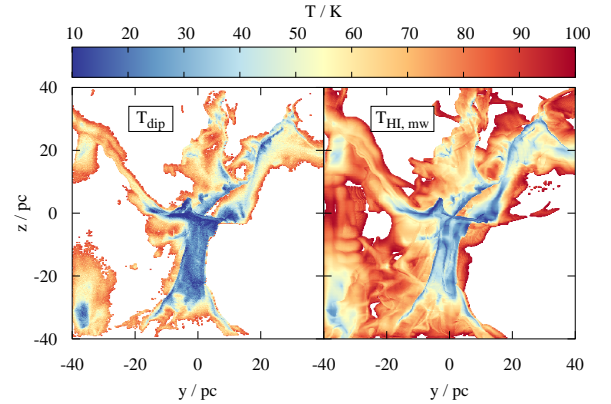


Figure 6. Map of T_{dip} (left, Eq. 10), which can be used such that Eq. 3 yields a result for every velocity channel, and the mass-weighted average of the temperature of the HI gas (right) for the same snapshot as shown in Fig. 4. Both quantities show a reasonable agreement within about 20 K. However, T_{dip} is quite low in the central areas. This explains the poor match of the observed with the actual column density (Fig. 4), as here often $T_{\text{HISA}} > T_{\text{dip}}$ (depending on the actual choice of T_{HISA}).

$N_{\text{HI,obs}}$ on T_{HISA} , the actual value of $N_{\text{HI,obs}}/N_{\text{HI,real}}$ increases with increasing T_{HISA} at high T_{dip} (coloured lines in the bottom panel of Fig. 7).

(iii) $T_{\text{HISA}} \approx T_{\text{dip}}$: Only in a narrow range, where T_{dip} is comparable to the chosen T_{HISA} , the HI column density is determined with a

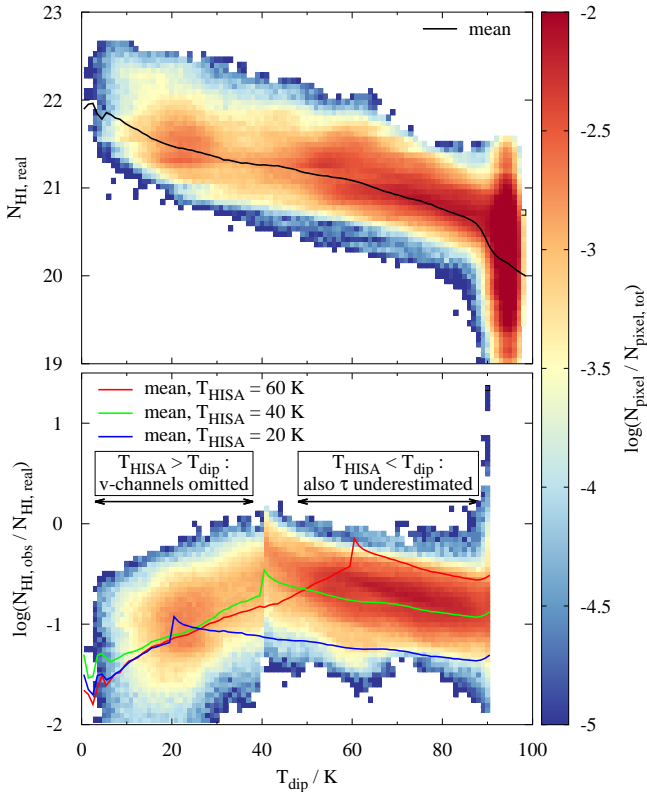


Figure 7. Top: Phase diagram of $N_{\text{HI,real}}$ vs. T_{dip} for the same snapshot as in Fig. 4. The highest HI column densities are associated with low T_{dip} . Bottom: Phase diagram of the ratio of $N_{\text{HI,obs}}$ and $N_{\text{HI,real}}$ vs. T_{dip} for the same snapshot as in the top panel using $T_{\text{HISA}} = 40$ K. The coloured lines show the mean value of the distribution for three different T_{HISA} . Overall the actual HI column density is underestimated by up to a factor of ~ 10 . Changing T_{HISA} increases the accuracy only locally, i.e. where that assumed T_{HISA} roughly corresponds to T_{dip} , which represents the real temperature of the HISA feature. We indicated the reasons of the underestimation in the two temperature ranges above and below $T_{\text{dip}} = T_{\text{HISA}}$.

reasonable accuracy. This is due to the fact that T_{dip} is a proxy for the real temperature of the HISA feature and thus well described by the choice of T_{HISA} . Changing T_{HISA} improves the accuracy only locally, i.e. the peak of the coloured lines in the bottom panel of Fig. 7 is shifted horizontally.

Overall, our results demonstrate that finding an accurate value for T_{HISA} is crucial but at the same time *not possible* when using a single value for the entire map. In addition, both under- and overestimating T_{HISA} leads to an underestimation of the HI column density. Moreover, the significant variations of $T_{\text{HI,mw}}$ across the map (right panel of Fig. 6) indicate that similar variations also occur for each individual pixel *along* the LOS. Hence, even for an individual pixel the assumption of a constant T_{HISA} presents an oversimplification, which in turn results in the observed underprediction of the HI column density particularly for the dense regions.

The rather low HI temperatures found in our simulations ($\lesssim 40$ K, Fig. 6) are in good agreement with a number of observations of Galactic MCs, which find typical HI temperatures between 10 K and 40 K (Gibson et al. 2000; Kavars et al. 2003, 2005; Klaassen et al. 2005; Fukui et al. 2014, 2015; Stanimirović et al. 2014; Dénes et al. 2018). They are, however, lower than typical temperatures found by

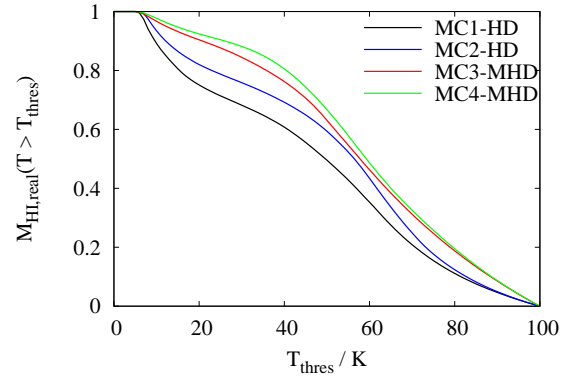


Figure 8. Cumulative temperature PDF showing the amount of cold HI above a certain threshold temperature for all four MCs at $t_{\text{evol}} = 2$ Myr. The steady rise with decreasing temperature indicates that no single temperature choice for T_{HISA} is suitable to accurately determine the amount of cold HI in the clouds. Note that gas above 100 K is not considered here.

Wang et al. (2020b) in the giant molecular filament GMF38a. A possible reason for this might be stellar feedback heating the gas in GMF38a. In consequence, the HI column densities determined in Wang et al. (2020b) might be more accurate than in our case.

The non-isothermality of the cold HI gas is further emphasised when considering its temperature distribution in Fig. 8 showing the cumulative PDF of HI gas above a certain threshold temperature for all four MCs at $t_{\text{evol}} = 2$ Myr. The amount of HI gas is rising steadily with decreasing temperature, independent of the considered MC. This shows that no *single* temperature can be used to describe the HI content of MCs. As an example, for $T_{\text{HISA}} = 40$ K, the HISA observations would (at least) miss out 20 – 40% of the cold HI mass.

The above results explain why also in the absence of observational effects like noise and limited spectral or spatial resolution the poor match between the observed and actual HI column density remains (see Fig. A1 in Appendix A). Also for different assumed distances of 150 pc and 3 kpc we find little differences. This further supports our claim that the underestimation of $N_{\text{HI,real}}$ can be attributed – at least in parts (see Section 3.3) – to the non-uniform HI temperatures present in the clouds.

3.3 The HI optical depth

In order to investigate the typical optical depths in our clouds, in Fig. 9 we plot a proxy for the HI optical depth, $\langle \tau \rangle$, for MC1-HD at 2 Myr. The definition of $\langle \tau \rangle$ is given in Appendix B. It represents a channel-averaged approximation to the real optical depth which is accurate within a few 10% above $\langle \tau \rangle = 1$, i.e. in the optically thick regions we are interested in here. For optically thin regions, the approximation is not applicable, which is why we do not show these regions here. The values of $\langle \tau \rangle$ span a wide range, from the moderately optically thick regime up to highly optically thick regions with $\langle \tau \rangle \sim 10$. In particular, the entire area of central cloud (compare with bottom middle panel of Fig. 2) has an optical depth $\gtrsim 1$, which is in excellent agreement with recent observations (e.g. Fukui et al. 2014, 2015; Bihr et al. 2015; Dénes et al. 2018; Murray et al. 2018; Syed et al. 2020; Wang et al. 2020b). Our results thus demonstrate that optical depth effects cannot be neglected in HI observations of MCs, e.g. also when calculating N_{HI} from HI emission observations. We note that at first view the maximum values of $\langle \tau \rangle$ around a few 10

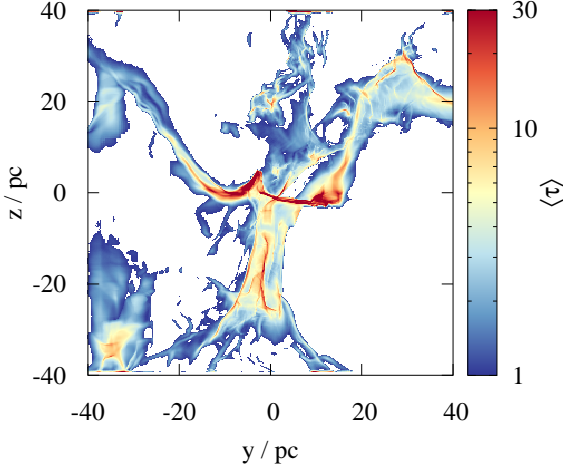


Figure 9. Map of the HI optical depth proxy $\langle \tau \rangle$ (see Appendix B) for MC1-HD at 2 Myr. The dense cloud region (compare with bottom middle panel of Fig. 2) has an average optical depth ≥ 1 , thus optical depth corrections cannot be neglected when calculating HI column densities.

appear high in comparison with those found in the aforementioned observational works. However, as these measurements are limited by observational noise, ΔT , the observationally reported values have to be taken as lower limits (see e.g. fig. 10 of Bihr et al. 2015).

The partly very high optical depths give rise to an additional source of error, which can result in the observed underestimation of $N_{\text{HI,real}}$ (Fig. 5). This error is related to the observational noise ΔT , whose effect becomes particularly pronounced in regions with very high optical depths. In these regions, the observed brightness temperature T_{on} will be close to the actual temperature T_{HISA} of the absorbing, cold HI layer, which is equivalent to $T_{\text{off-on}} \approx 100 \text{ K} - T_{\text{HISA}} - \Delta T$ (Eq. 5). Inserting this value into Eq. 6 yields

$$\tau_{\text{HISA,noise}} = -\ln \left(1 - \frac{100 \text{ K} - T_{\text{HISA}} - \Delta T}{100 \text{ K} - T_{\text{HISA}}} \right) = -\ln \left(\frac{\Delta T}{100 \text{ K} - T_{\text{HISA}}} \right). \quad (11)$$

Analysing Eq. 11 shows that also the observational uncertainty ΔT in highly optically thick regions results in an underestimation of $N_{\text{HI,obs}}$ regardless of its sign:

(i) $\Delta T < 0$: If noise artificially lowers T_{on} , this *increases* $T_{\text{off-on}}$ beyond a value of $100 \text{ K} - T_{\text{HISA}}$ in a highly optically thick region. Hence, Eq. 11 would contain a negative expression in the logarithm and the contribution from the corresponding velocity channel has to be omitted.

(ii) $\Delta T > 0$: If noise, but also the potential emission of warm and diffuse HI in the foreground, increases T_{on} (and thus decreases $T_{\text{on-off}}$), this results in an underestimation of the true value of τ_{HISA} (which can be larger than $\tau_{\text{HISA,noise}}$) and thus also $N_{\text{HI,obs}}$ (Eq. 7). The effect of foreground emission is thus also related to the problem of identifying T_{HISA} correctly.

Hence, even if one were to choose the correct value of T_{HISA} , $N_{\text{HI,obs}}$ is on average underestimated in optically thick regions. This is indeed shown by the coloured lines in the bottom panel of Fig. 7, which represent the average value of $N_{\text{HI,obs}}/N_{\text{HI,real}}$ as a function of T_{dip} : Even at the peaks of the curves, where $T_{\text{HISA}} \approx T_{\text{dip}}$, the real HI column density is on average underestimated. We emphasise that this underestimation due to ΔT adds on top of the problem to determine a reasonable value of T_{HISA} . This effect can also explain why for lower

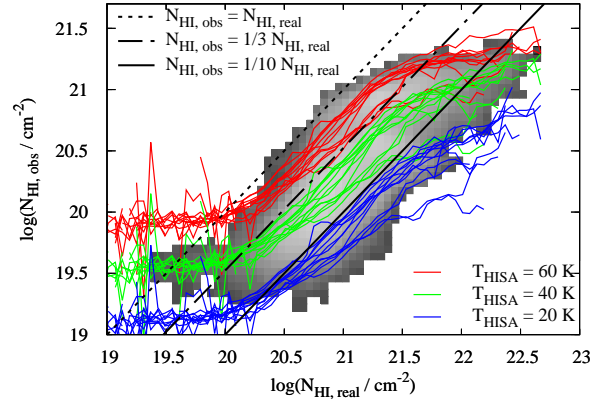


Figure 10. Same as in Fig. 5 but now including the correction in optically thick regions (see text). Overall, the match is somewhat improved. However, depending on the choice of T_{HISA} , $N_{\text{HI,real}}$ is still underestimated by a factor of a few up to ~ 10 in particular in the densest regions.

values of T_{dip} , the underestimation becomes more severe (bottom panel of Fig. 7): the lower T_{dip} , the higher is the HI column density and thus the optical depth, which amplifies the issue arising from this effect. Furthermore, it also explains the artificial levelling-off of $N_{\text{HI,obs}}$ around 10^{21} cm^{-2} which occurs at high $N_{\text{HI,real}}$ (Fig. 5), i.e. where the optical depth is naturally high.

3.3.1 Opacity correction in MCs

Motivated by the large extent of optically thick regions in MCs (Fig. 9), we suggest a method to improve the accuracy of $N_{\text{HI,obs}}$: A significant underestimation occurs in the high- N_{HI} /high-optical depth regions of the MCs, where Eq. 6 yields no result for τ_{HISA} any more and velocity channels have to be omitted (see Fig. 7). Hence, for these velocity channels we use an optical depth set by the typical rms noise (ΔT) of the observation, which is given by $\tau_{\text{HISA,noise}}$ (Eq. 11), e.g. for $T_{\text{HISA}} = 40 \text{ K}$ and the adopted noise of 3 K (Section 2.2.1), we obtain $\tau_{\text{HISA,noise}} = 2.6$. We emphasise that this estimate is still a conservative estimate as the actual optical depth is likely to be higher. A similar approach is also followed by Bihr et al. (2015) for HI emission maps.

The obtained column density maps are shown in Fig. A2 in Appendix A. As can be seen, $N_{\text{HI,obs}}$ in the denser parts of the MCs is represented better than before (compare with Fig. 4). In the very densest parts, however, $N_{\text{HI,real}}$ is still significantly underestimated. This is also visible in Fig. 10, where we show the mean values of $N_{\text{HI,obs}}$ for all MCs and directions at 2 Myr using this correction. There is an improvement in all areas compared to the case without any correction (see Fig. 5). However, $N_{\text{HI,real}}$ can still be underestimated by a factor of a few to ~ 10 . Hence, the suggested method has a moderate impact on increasing the accuracy, which we, as stated before, attribute to the fact that the assumed value of $\tau_{\text{HISA,noise}}$ is most likely lower than the real optical depth.

3.4 The cold HI budget of molecular clouds

Summarizing the findings of the previous sections we find that the uncertainty in determining the HI column density is due to (i) the assumption of a fixed temperature T_{HISA} for the calculation of the HISA column densities and (ii) noise in the temperature brightness measurement. As a consequence, either the optical depth and the

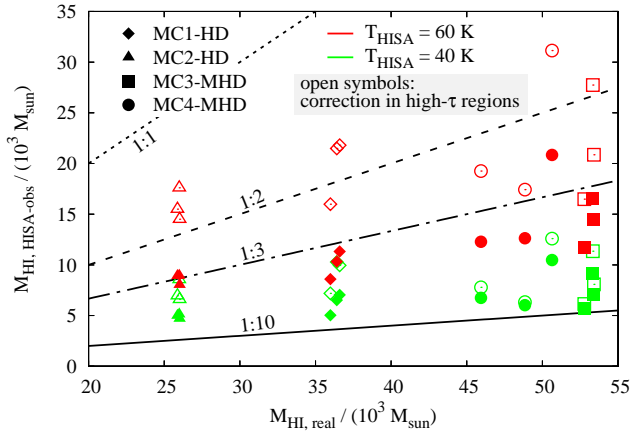


Figure 11. Accuracy of the HI mass inferred from HISA observations for the four different MCs at 2 Myr (symbols) for $T_{\text{HISA}} = 40$ K (green) and 60 K (red). The black lines show the different mass ratios to guide the readers eye. Overall, we find that the HI mass is underestimated by a factor of a few up to ~ 10 . Correction for optically thick channels (open symbols) improves the accuracy only moderately. Note that depending on the chosen projection direction, the mass in the observable area is different for the same MC.

true T_{HISA} are underestimated (mainly in the outer parts of MCs) or velocity channels have to be omitted for the calculation of the column density (mainly in the densest parts of MCs). Overall, this results in a significant underestimation of the actual HI column densities by a factor of 3 – 10 (and even more in the densest regions of clouds).

This is also reflected in the total mass of cold HI in MCs inferred from HISA observations, $M_{\text{HI,HISA-obs}}$, shown in Fig. 11. Here, we add up the observed HI mass of all pixels for which a HISA feature is identified (i.e. pixels outside the coloured regions in Fig. 4 are ignored) using $T_{\text{HISA}} = 40$ K and 60 K. For the actual mass, $M_{\text{HI,real}}$, we only take into account HI gas with $T < 100$ K, to which our HISA observations are sensitive to. As for the column densities, also the total, cold HI mass is typically underestimated by a factor of a 3 – 10, when no correction in the optically thick regions is applied (filled symbols). The correction (Section 3.3.1), however, improves the accuracy only moderately by a factor of ~ 1.5 – 2 (open symbols). We emphasise that increasing T_{HISA} to obtain apparently more accurate mass estimates should be considered with caution. This merely leads to an overestimation of N_{HI} at low column densities compensating the underestimation at high column densities (see Fig. 5 and also Section 3.5).

We emphasise that our results do not change significantly among the different MCs considered, i.e. whether or not dynamically important magnetic fields are present. This indicates that HISA observations in general tend to significantly underestimate the cold HI budget in MCs. This is markedly different to results for the diffuse ISM (on scales $\gtrsim 1$ pc), where Murray et al. (2015, 2017) find that HISA observations can trace the HI mass with an accuracy of a few 10%. We tentatively attribute this to the fact that the authors focus on diffuse HI structures, which have lower optical depths and are thus less prone to the measurement uncertainties mentioned in Section 3.3. Furthermore, HI masses obtained from emission observations (e.g. Bühr et al. 2015), which correct for the optical depth and which also implicitly take into account warm HI ($T > 100$ K, in our case 22 – 47%), might achieve more accurate HI masses, a topic not investigated in this study.

3.5 Deriving N_{HI} using T_{HISA} as a free parameter

As the assumption of a fixed T_{HISA} contributes significantly to the underestimation of the HI column density (Section 3.2), we next leave T_{HISA} as a free parameter. We determine its value as well as the optical depth assuming a Gaussian optical depth profile, i.e. inserting Eq. 9 in Eq. 5 and fitting the observed HI spectrum. In Fig. 12 we show the various quantities obtained by the approach for MC1-HD at 2 Myr and an assumed distance of 150 pc. For other directions, times, clouds, and the 3 kpc-distance case, we find qualitatively and quantitatively similar results.

Also when leaving T_{HISA} as a free parameter, we overall find a quite poor match between the observed and actual N_{HI} (second panel from the left in Fig. 12): The method tends to overestimate the column density in the outskirts of the clouds and underestimate it in the central, high-column density regions. This is a direct consequence of the fitted values of τ_0 and T_{HISA} shown in the two right panels of Fig. 12. Although the fitted values of T_{HISA} appear to be comparable to the mass-weighted mean temperatures (right panel of Fig. 6), the values for τ_0 show an unphysical behaviour: High values are found in particular in the outer, low-column density parts of the clouds, where the optical depth is actually expected to be lower than in the central parts. This failure of the fitting procedure can be attributed to the fact that τ_0 and T_{HISA} are degenerate. Overestimating T_{HISA} requires a higher τ_0 (and vice versa) to match the observed $T_{\text{off-on}}$ at the dip of the absorption spectrum (Eq. 5). Following Eq. 7, this directly leads to an overshooting of $N_{\text{HI,obs}}$. This is also what happens at low N_{HI} in the case of a fixed $T_{\text{HISA}} = 60$ K (bottom right panel of Fig. 4 and Fig. 5). Uncertainties in T_{HISA} or τ_0 can arise due to the following reasons:

- First, discriminating e.g. an optically thick from an optically thin HISA feature requires accurate information about the wings of the spectrum. However, due to the assumed spectral resolution of 1 km s^{-1} and in parts also the presence of multiple absorption components (red line in Fig. 3), no reliable information about the optical depth can be extracted from the spectra. We note that when repeating the method for the noiseless, high-resolution spectra (200 m s^{-1}), we obtain a similar poor match between $N_{\text{HI,obs}}$ and $N_{\text{HI,real}}$, which further supports that the poor match is in parts related to the occurrence of multiple components.
- Second, as discussed in Sections 3.2 and 3.3, strong temperature variations along the LOS and the effect of noise in high optical depth regions complicate the accurate determination of T_{HISA} and thus τ_0 .

This suggests that, in order for this method to work, multiple Gaussian components have to be taken into account for the fitting procedure, which we do not follow further here.

Given the similarity of T_{dip} and the mass-weighted HI temperature $T_{\text{HI,mw}}$ (see Fig. 6), we also try an alternative approach by setting T_{HISA} close to, but slightly below T_{dip} . In detail, we set

$$T_{\text{HISA}} = T_{\text{dip}} - \Delta T \quad (12)$$

with $\Delta T = 3$ K being the noise level of the synthetic observations and test the approach for MC1 at $t_{\text{evol}} = 2$ Myr. Overall, we find a qualitatively similar poor match between $N_{\text{HI,obs}}$ and $N_{\text{HI,real}}$ as for the method from Knapp (1974) explored before. At low $N_{\text{HI,real}}$ the observed column density is significantly too high, whereas at high $N_{\text{HI,real}}$ it is consistently too low (not shown). In consequence, also the spatial distribution of HI inferred with this method does not match, even qualitatively, the actual distribution (similar to that in the left panel of Fig. 12). Overall, the reasons for this poor match are again the temperature variations along the LOS (Section 3.2), the

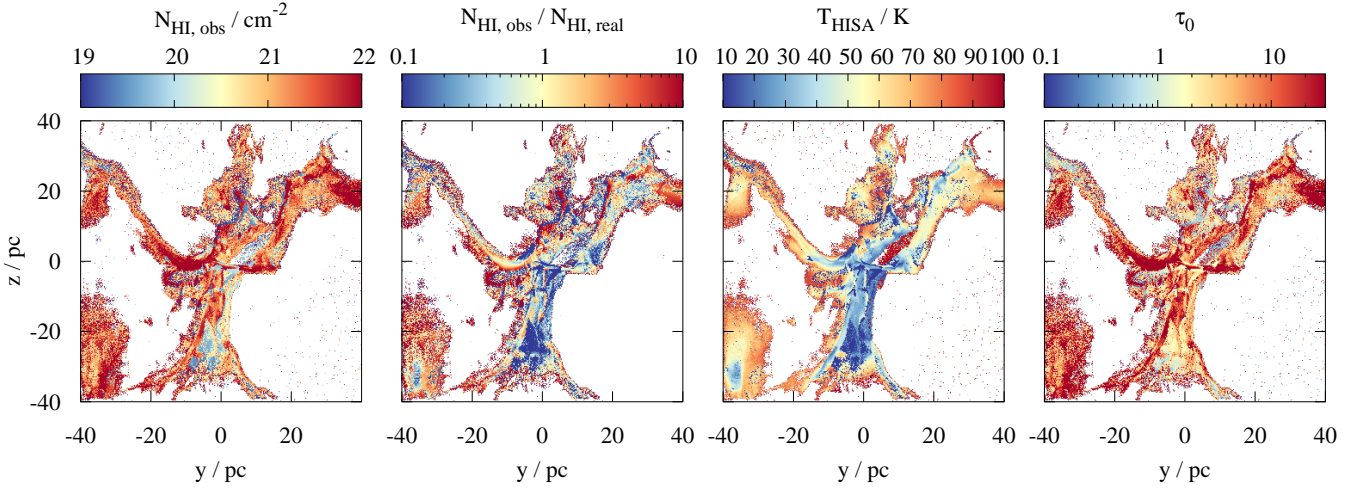


Figure 12. Maps of $N_{\text{HI,obs}}$ and its ratio to the actual HI column density (two left panels) determined by leaving T_{HISA} and τ_0 (two right panels) as free parameters. The maps are shown for the same snapshot as in Fig. 4. Overall, allowing T_{HISA} to be a free parameter does not increase the accuracy compared to assuming a fixed T_{HISA} (compare Fig. 4). Although the determined T_{HISA} is similar to the mass-weighted HI temperature (right panel of Fig. 6), the optical depth shows a partly unphysical behaviour with high values in the outer, low-column density areas.

partly high optical depths (for the high- N_{HI} regions, Section 3.3) as well as the degeneracy of T_{HISA} and τ_{HISA} (for the low N_{HI} regions, this section). In summary, we find that, even when leaving T_{HISA} as a free parameter, the quality of the obtained HI column density maps does not increase, but partly even decreases.

3.6 The HI velocity dispersion

Finally, we consider the accuracy of the HI velocity dispersion inferred from HISA observations. For this purpose, we compare the non-thermal velocity dispersion σ_{obs} identified via the BTS tool (Section 2.3) with the actual HI velocity dispersion along each LOS directly inferred from the simulation data, σ_{real} . For σ_{real} we only take into account the velocity component along the LOS and HI with a temperature below 100 K and then calculate for each pixel the HI mass-weighted LOS average. For σ_{obs} we correct the value obtained by BTS, σ_{BTS} , for the contribution from the limited channel width of 1 km s^{-1} and thermal motions, i.e.

$$\sigma_{\text{obs}} = \left(\sigma_{\text{BTS}}^2 - \left(\frac{1 \text{ km s}^{-1}}{\sqrt{8 \log 2}} \right)^2 - c_s^2 \right)^{1/2}, \quad (13)$$

with c_s being the sound speed for HI gas, where, for simplicity, we assume an average temperature of 40 K (right panel of Fig. 6). The factor $\sqrt{8 \log 2}$ accounts for the conversion of channel width into the standard deviation. In the following we only consider pixels where $\sigma_{\text{obs}} > 0$.

In the left and middle panel of Fig. 13 we plot the distribution of σ_{real} and σ_{obs} and its mean value (black line) as a function of $N_{\text{HI,real}}$ for MC1-HD at $t_{\text{evol}} = 2 \text{ Myr}$ for one direction assuming a distance of 150 pc for the beam size. We note that the following results also hold for the other clouds and times. First, we find that the scatter for σ_{real} appears to be somewhat larger than for σ_{obs} . Second, for σ_{real} there is only a moderate increase with $N_{\text{HI,real}}$ in particular for $N_{\text{HI,real}} > 10^{21} \text{ cm}^{-2}$, whereas for σ_{obs} the increase is more pronounced. The latter could be attributed to opacity broadening occurring for high $N_{\text{HI,real}}$ (see black line in Fig. 3), which we expect to happen frequently, given the high optical depths found in

our MCs (Fig. 9). The presence of multiple Gaussian components in the spectrum (red line in Fig. 3), however, can not explain the somewhat larger values of σ_{obs} compared to σ_{real} : Although the result of the single-component fit for σ_{BTS} will be broader than the velocity dispersion of the individual HI components, multiple components will also increase σ_{real} . We also note that the non-thermal velocity dispersions of HI of a few 1 km s^{-1} reported here are in general in agreement with the velocity dispersion of dense gas ($n > 100 \text{ cm}^{-3}$) in these clouds (Seifried et al. 2017).

The black lines in the right panel of Fig. 13 show the mean of $\log(\sigma_{\text{obs}}/\sigma_{\text{real}})$ for all clouds and projection directions at 2 Myr and an assumed distance of 150 pc. Despite the differences seen in the left and middle panel, σ_{obs} appears to trace the actual velocity dispersion with a reasonable accuracy. For $N_{\text{HI,real}} \lesssim 10^{22} \text{ cm}^{-2}$, the mean of $\log(\sigma_{\text{obs}}/\sigma_{\text{real}})$ is one average within ± 0.3 dex around a value of 0, which would indicate a perfect agreement. Also the standard deviations of the various distributions (grey lines) are about 0.2 – 0.3 dex. Hence, we argue that for typical HI column densities between $\sim 10^{20} \text{ cm}^{-2}$ and $\sim 10^{22} \text{ cm}^{-2}$, HISA observations are able to probe the non-thermal velocity dispersion of HI with an accuracy of a factor of ~ 2 , even in the case of a limited spectral resolution of $\sim 1 \text{ km s}^{-1}$. Only for very high HI column densities ($N_{\text{HI,real}} > 10^{22} \text{ cm}^{-2}$) the non-thermal velocity dispersion might be somewhat overestimated, which we tentatively attribute to the aforementioned opacity broadening of the absorption feature. We note that these results also hold for $t_{\text{evol}} = 3 \text{ Myr}$ and an assumed distance of 3 kpc.

Finally, in Fig. 14 we show the distribution of the Mach numbers $\sqrt{3}\sigma/c_s$ (assuming $T = 40 \text{ K}$) for MC1-HD at 2 Myr. The values are inferred directly from the simulation using σ_{real} (black lines) and from the HISA observation using σ_{obs} (red lines). For other clouds, we find similar results. Overall, the HI gas is moderately supersonic with the distribution peaking around Mach numbers of a few although also values up to ~ 10 are reached. The observationally determined Mach numbers somewhat underrepresent the lowest values. This could be related to the aforementioned opacity broadening or a broadening due to the limited spectral resolution. The overall similarity between both distributions, however, confirms the accuracy of

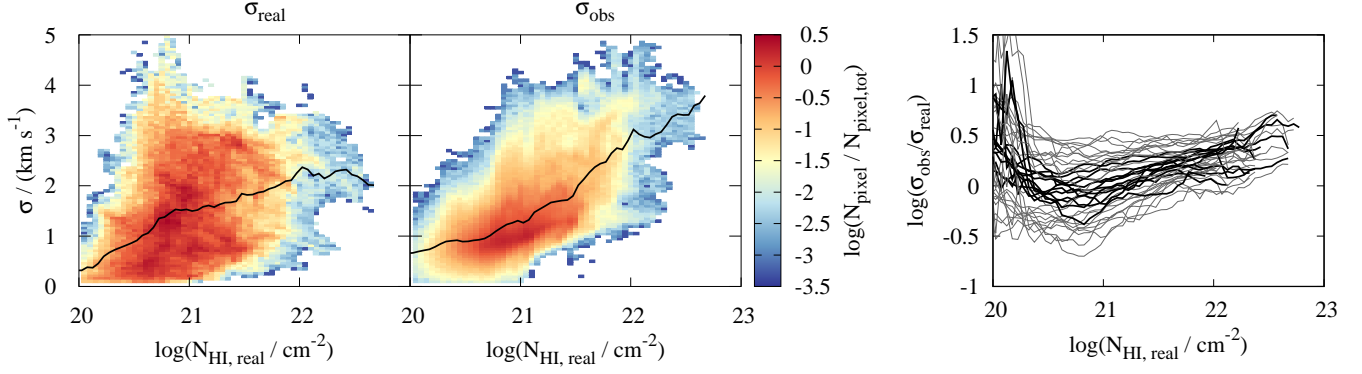


Figure 13. Left and middle panel: Distribution of the real non-thermal HI velocity dispersion, σ_{real} , and the observed one, σ_{obs} , as a function of $N_{\text{HI,real}}$ for MC1-HD at $t_{\text{evol}} = 2$ Myr for one direction assuming a distance of 150 pc. Overall, there is an increase of σ with the column density although the effect is less pronounced for σ_{real} . The stronger increase of σ_{obs} could be due to opacity broadening. Right panel: Ratio of σ_{obs} and σ_{real} as a function of $N_{\text{HI,real}}$. The black line shows the mean for all clouds and three directions at $t_{\text{evol}} = 2$ Myr assuming a distance of 150 pc, the grey lines represent the interval of one standard deviation. Overall, HISA observations trace the velocity dispersion with an accuracy of a factor of ~ 2 .

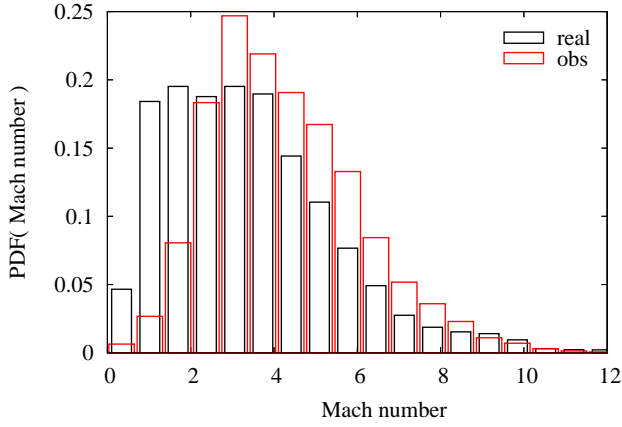


Figure 14. Mach number distribution of the HI gas for the same snapshot as in Fig. 4 assuming a temperature of 40 K. The black lines shows the distribution obtained from the simulation data directly (σ_{real}), the red that from the observed velocity dispersion (σ_{obs}). The HI gas is moderately supersonic with Mach numbers around 1 – 10.

a factor of ~ 2 between σ_{real} and σ_{obs} reported before. Furthermore, the Mach numbers found are also in good agreement with recent HISA observations (Burkhart et al. 2015; Syed et al. 2020; Wang et al. 2020b).

4 DISCUSSION

4.1 The N_{HI} -PDF: Comparison with observations

As discussed in Section 3.1, we find that HISA measurements tend to underestimate the actual column density of cold HI by a factor of 3 – 10 in the outer parts of MCs and potentially by an even higher factor in the central, high density parts. We attribute this to (i) a large temperature variation of the HI gas and the assumption of a fixed T_{HISA} and (ii) the effect of noise in the brightness temperature measurements in particular for regions of high optical depth.

This underestimation is again demonstrated in Fig. 15 where we

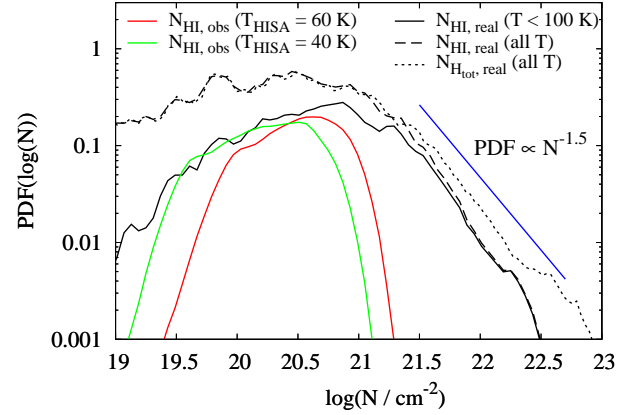


Figure 15. Column density PDFs of the cold HI (black solid line), the total HI (black dashed line), and all hydrogen nuclei (H_{tot} , black dotted line) inferred directly from the simulation of MC1-HD at 2 Myr for one direction. In addition, the corresponding PDFs determined from the synthetic HISA observations assuming $T_{\text{HISA}} = 40$ and 60 K (green and red line, respectively) are shown. The $N_{\text{HI,obs}}$ -PDFs peak at significantly lower values than that of $N_{\text{HI,real}}$ and show a roughly lognormal distribution. In contrast, the $N_{\text{HI,real}}(N_{\text{H,tot}})$ -PDFs exhibit a power-law tail roughly proportional to $N^{-1.5}$ (blue line), which indicates that also HI is gravitationally unstable.

show the area-weighted PDFs of $N_{\text{HI,real}}$ and $N_{\text{HI,obs}}$ for MC1-HD at $t_{\text{evol}} = 2$ Myr for one direction at an assumed distance of 150 pc⁶. The latter is derived for $T_{\text{HISA}} = 40$ and 60 K (coloured lines). As expected, the peak of the $N_{\text{HI,obs}}$ -PDF is shifted by a factor of 3 – 10 towards lower column densities with respect to that of the $N_{\text{HI,real}}$ -PDF (black solid line). Moreover, also the shapes of the two PDFs are very different with important implications. First, the $N_{\text{HI,real}}$ -PDF is significantly broader than the $N_{\text{HI,obs}}$ -PDF. This indicates

⁶ We note that the integrated area under the curves are not necessarily unity as many pixels have no observed HI column density (Fig. 4). Hence, the relative area under the curves gives the reader a direct indication of how many pixels are omitted (i.e. have $N_{\text{HI,obs}} = 0$) compared to the PDF of all HI.

that the width of the $N_{\text{HI,obs}}$ -PDF obtained from HISA observations might not be a good quantity to assess turbulence statistics (see e.g. Burkhart & Lazarian 2012, for an application to the $N_{\text{HI,tot}}$ -PDF). Second, the $N_{\text{HI,real}}$ -PDF shows signs of a power-law tail at column densities above a few 10^{21} cm^{-2} , which is roughly proportional to $N^{-1.5}$, similar to that of the $N_{\text{HI,tot}}$ -PDF (black dotted line, see also Kainulainen et al. 2009; Kritsuk et al. 2011; Girichidis et al. 2014; Schneider et al. 2015; Auddy et al. 2018; Veltchev et al. 2019). This power-law tail indicates that also the dense HI gas is undergoing gravitational collapse. We emphasise, however, that – as the dense gas ($N \gtrsim 10^{21} \text{ cm}^{-2}$) is predominantly molecular (bottom panel of Fig. 1) – the gravitational force in this range is dominated by gas in form of H_2 with which the HI is mixed.

Our $N_{\text{HI,real}}$ -PDF are markedly different from PDFs found in recent HISA observations (Burkhart et al. 2015; Imara & Burkhart 2016; Syed et al. 2020; Wang et al. 2020b) which find a log-normal shape indicating that the cold HI is not gravitationally unstable. This apparent contradiction could have its origin in possible observational biases, indicated by some striking similarities between our synthetic HI observations and that of the aforementioned authors: Our synthetic and the actually observed $N_{\text{HI,obs}}$ -PDF are of roughly lognormal shape, are in a similar range ($N_{\text{HI}} = 10^{20-21} \text{ cm}^{-2}$), and are at significantly lower column densities than that of either H_2 and the total HI observed in emission (Syed et al. 2020; Wang et al. 2020b) or that of $N_{\text{HI,tot}}$ measured via dust emission (Burkhart et al. 2015; Imara & Burkhart 2016). Taking these similarities into account, we suggest that there indeed is an observation bias in the shape of observed N_{HI} -PDFs. This could be particularly pronounced at the high end of the PDF, which is often characterised by a power-law. In addition, the N_{HI} values obtained should rather be considered as lower thresholds. We note, however, that an MC at an very early evolutionary stage might not have undergone gravitational collapse, i.e. might not yet have developed high column densities ($\gtrsim 10^{21} \text{ cm}^{-2}$) and the associated power-law tail in the N -PDF. Therefore, for such an MC, the assessment of the HI column densities and masses via HISA observations might still be somewhat better compared to the findings presented here.

4.2 Multiple HI- H_2 transitions: Comparison with analytical results

As stated before, recent semi-analytical works predict that, for ISM conditions comparable to that of the solar neighbourhood, the transition from HI to H_2 occurs at column densities of $\lesssim 10^{21} \text{ cm}^{-2}$ (Krumholz et al. 2008, 2009; Sternberg et al. 2014; Bialy & Sternberg 2016). These models also suggest an upper limit of N_{HI} around this value. Contrary to that, for the clouds simulated in this work, we find HI column densities partly well above this value (see Figs. 1 and 2). Also recent observations of W43 (Motte et al. 2014; Bihl et al. 2015) and clouds outside the Galactic plane (Fukui et al. 2014, 2015) and a reinterpretation of HI observations of Perseus (Okamoto et al. 2017) have revealed HI column densities of up to a few 10^{22} cm^{-2} , thus well comparable to our findings, but in apparent contradiction to the theoretical predictions. Furthermore, also observations of the Magellanic Clouds by Welty et al. (2012) seem to challenge the prediction for the value of $N_{\text{HI,tot}}$, where the transition to H_2 dominated gas is supposed to occur (Krumholz et al. 2008, 2009; McKee & Krumholz 2010).

However, strictly speaking the suggested, upper limit around 10^{21} cm^{-2} only applies to a single HI- H_2 transition. As pointed out by Motte et al. (2014), a possible solution for this contradic-

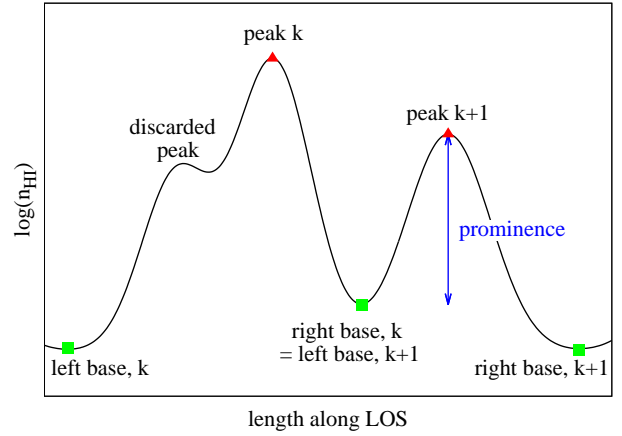


Figure 16. Sketch for the identification of HI peaks (red triangles) and the position of their bases (green squares), also for a case where a local peak is discarded. The blue arrow indicates the prominence of peak k+1.

tion could thus be the presence of several transitions along the LOS (see also Bialy et al. 2017a). Indeed, the highly complex structure of our simulated MCs (see Fig. 2) and of real, observed clouds indicates that the assumption of a single HI- H_2 transition might be an oversimplification and that rather several transitions are present.

In order to test whether the high HI column densities in our simulated MCs can be attributed to several HI- H_2 transitions, we identify the number of HI-density peaks along rays which intersect the entire length of the zoom-in regions and which are distributed uniformly over the entire area of the emission maps with a spacing of 0.24 pc. For this purpose, we determine the profile of the logarithm of the HI density, $\log(n_{\text{HI}})(l)$, along each ray, i.e. along the LOS of each pixel. A few selected profiles are shown in Fig. A4, demonstrating their variability for different pixels, which necessitates a more systematic study.

For this purpose, we first identify the positions of the peaks of $\log(n_{\text{HI}})$ along the LOS, $l_{\text{peak},k}$, as well as the position of their left and right base, $l_{\text{base,left},k}$ and $l_{\text{base,right},k}$, respectively (see Fig. 16 for a schematic view). The base of a peak (green squares) is the minimum of the density profile between this and the neighbouring peak. Furthermore, in order to account for the influence of small-scale density fluctuations, we discard peaks which (i) have a prominence (blue arrow) of less than 0.5 (in log-space), or (ii) have a peak height $\log(n_{\text{HI,peak}})$ of less than 0.5 ($n_{\text{HI,peak}} \approx 3 \text{ cm}^{-3}$), or (iii) are separated from the next (and higher) peak by less than 2 grid cells along the LOS⁷. Finally, we note that as n_{HI} comes from the chemical network implemented in the simulations, a low n_{HI} could indicate either a low total gas density or a high gas density, where hydrogen is already predominantly in form of H_2 .

Next, we calculate the column density of each HI-density peak as

$$N_{\text{HI,peak},k} = \int_{l_{\text{base,left},k}}^{l_{\text{base,right},k}} n_{\text{HI}} dl, \quad (14)$$

⁷ When we discard a peak, the minimum between this discarded and the neighbouring peak k , is *not* taken as the base of the peak k . Rather, the base of the peak k is shifted beyond the discarded peak such that the discarded peak now lies between $l_{\text{base},k}$ and $l_{\text{peak},k}$ (see left-most green square in Fig. 16). We also note that we tested the approach by discarding the lower of two peaks when they are separated by less than 4 cells. This, however, affected the findings only marginally, which is why we do not follow this further here.

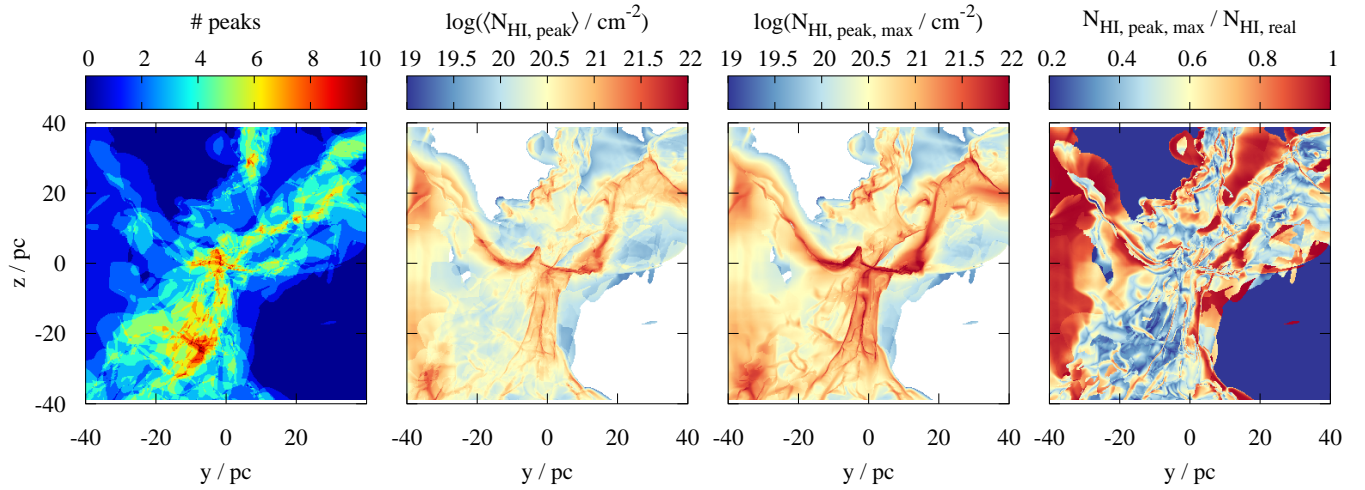


Figure 17. Maps of the number of HI-density peaks per LOS, the mean HI column density per HI-density peak, the HI column density of the most prominent HI-density peak and the ratio of this value to the total HI column density (from left to right). The left-most panel demonstrates the occurrence of up to 10 peaks, which corresponds to the same number of HI-H₂ transitions along the LOS. In consequence, the average HI column density per peak (center-left panel) mostly matches the theoretical predictions of $\lesssim 10^{21} \text{ cm}^{-2}$. However, the most prominent HI-density peak (center-right panel) often has a column density that is considerably larger than this value and contributes significantly to $N_{\text{HI,real}}$ ($\gtrsim 40\%$, right panel).

and determine the average column density, $\langle N_{\text{HI,peak}} \rangle$, of all peaks along a given LOS. In addition, we identify the most massive peak, i.e. the peak which accumulates most of the HI along the given LOS, and determine its column density, $N_{\text{HI,peak,max}}$. In Fig. 17, we plot the number of peaks along each LOS, $\langle N_{\text{HI,peak}} \rangle$, $N_{\text{HI,peak,max}}$ and the ratio $N_{\text{HI,peak,max}}/N_{\text{HI,real}}$ for MC1-HD at 2 Myr along one direction. The last value shows how much the most massive peak contributes to the overall HI column density.

The left panel of Fig. 17 shows that there are indeed up to ~ 10 HI-density peaks along the LOS as suggested by Bialy et al. (2017a) for the case of W43. There is a moderate tendency of a higher number of peaks towards the center of the MC, i.e. with increasing $N_{\text{HI,real}}$, probably caused by the filamentary substructure of the MCs. This increase causes $\langle N_{\text{HI,peak}} \rangle$ to remain below 10^{21} cm^{-2} for the vast majority of rays (second panel of the left), only for about 5 – 25% of all rays (depending on the cloud, direction, and time) it exceeds this value. Hence, on first view this appears to be in rough agreement with analytical predictions (Krumholz et al. 2008, 2009; Sternberg et al. 2014; Bialy & Sternberg 2016).

However, the column density of the dominant peak, $N_{\text{HI,peak,max}}$, exceeds the value of 10^{21} cm^{-2} for a large number of rays (second panel from the right). We find that $N_{\text{HI,peak,max}}$ exceeds 10^{21} cm^{-2} for 30 – 50% of the rays, i.e. more than twice as often as the corresponding fraction for $\langle N_{\text{HI,peak}} \rangle$. Again, the exact fraction depends on the considered MC, direction, and time. However, we do not see any dependence on the presence or absence of magnetic fields in the simulations, despite the fact that the field is dynamically important for the overall (chemical) evolution of the MCs (see Seifried et al. 2020a,b). Furthermore, the dominant peak accounts on average for about 40 – 60% and even more of $N_{\text{HI,real}}$ (right panel) and is thus indeed dominating the overall HI budget of the clouds. Hence, these findings are in contrast to the theoretical models, and we will discuss their implications in detail in the following section.

5 IS THERE MORE COLD HI THAN THOUGHT?

5.1 The theoretical perspective

As discussed so far, our results indicate that semi-analytical models tend to underestimate the maximum column density of cold HI in MCs. This can be attributed to several reasons. First, as suggested by Motte et al. (2014) and Bialy et al. (2017a) and explicitly shown here for the first time, in realistic models of MCs there appear up to ~ 10 HI-H₂ transitions along the LOS. Secondly, non-equilibrium effects can increase the HI content of MCs due to the limited time available for H₂ to form (Glover & Mac Low 2007b; Glover et al. 2010; Mac Low & Glover 2012; Motte et al. 2014). We investigate this effect by artificially evolving the chemistry for a selected snapshot to chemical equilibrium (see Appendix A for details). Doing so, we find that this reduces the HI content in our MCs by a factor of 2 – 2.5 (see Fig. A3). Hence, the assumption of chemical equilibrium in semi-analytical models indeed results in too low HI abundances compared to the actual non-equilibrium HI present in dynamically evolving MCs.

In addition, we here suggest a third reason why even for a single HI-H₂ transition N_{HI} could be higher (center-right panel of Fig. 17) than predicted by semi-analytical models with a 1-dimensional geometry (Krumholz et al. 2008, 2009; Sternberg et al. 2014; Bialy & Sternberg 2016). For this purpose we consider the effect of assuming an idealised plane-parallel slab in more detail. In such a configuration the gas in the cloud is irradiated only from one side, i.e. a parcel of gas having a high column density in the slab direction will receive very little radiation. In other words, for a plane-parallel slab – at a given total hydrogen nuclei column density $N_{\text{H,tot}}$ towards the direction of the incident radiation – the extinction is maximal as radiation coming from other possible directions is neglected. In consequence, also the amount of HI is minimal due to the lack of H₂ dissociation. The same chain of arguments can also be made for a spherically symmetric configuration.

In contrast, under realistic conditions in turbulent MCs, there may exist large low-density voids through which the radiation can propagate into the cloud (almost) unhindered. This is sketched in the left

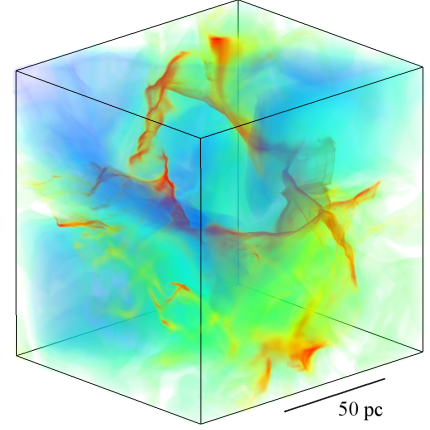
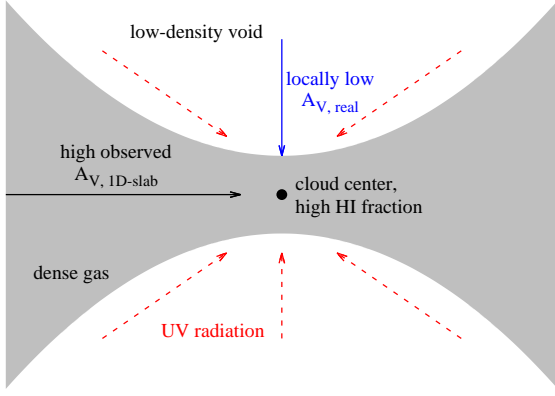


Figure 18. Left: Sketch of a situation in a MC (dense gas depicted with grey). Here, the observer’s assumption of a 1-dimensional, plane-parallel configuration as applied in semi-analytical models overestimates the shielding (black arrow, $A_{V,1D-slab}$) and thus underestimates the amount of HI in the cloud’s center. Under realistic conditions, radiation (red arrows) dissociating H_2 might be able to propagate through low-density voids (white areas) towards the center of the cloud. This results in a rather low actual visual extinction, $A_{V,real}$. Right: Volume rendering of MC1-HD at 2 Myr showing the highly complex and filamentary structure of the dense gas (reddish). Large low-density voids (bluish) are recognisable through which radiation can propagate into the cloud thus increasing the HI fraction. This resembles the simplified picture shown in the left panel.

panel of Fig. 18: a dense region shielded completely against UV radiation from one direction (horizontal) can still be irradiated from another direction (vertical). Hence, if observed from the horizontal direction, this region would *appear* completely optically thick (i.e. a high value of $A_{V,1D-slab}$), corresponding to the assumption of a plane-parallel configuration. In reality, however, the region might still receive up to $\sim 50\%$ of the radiation coming from the vertical direction, i.e. the real A_V might be significantly lower⁸. In consequence, H_2 might still be dissociated by UV radiation even in the central regions of MCs thus increasing the amount of HI. Considering a 3-dimensional graphical representation of MC1-HD at 2 Myr (right panel of Fig. 18) indeed shows that there exist these large low-density voids (bluish) through which radiation can travel (almost) unattenuated thereby dissociating H_2 in the densest regions (reddish). We note that also for internal, stellar radiative feedback the actual cloud’s substructure and shielding parameters have a similar importance (Haid et al. 2019).

One could interpret this effect as either increasing the radiation strength or decreasing the *effective* shielding of UV radiation in the cloud. In the semi-analytical models of Sternberg et al. (2014), Bialy & Sternberg (2016) and Bialy et al. (2017b), this is parametrised by their parameter αG . There, α indicates the radiation strength and G the shielding factor including H_2 self-shielding and dust attenuation; the lower G , the better the radiation is shielded. We speculate that large density voids can easily reduce the (self-)shielding of the surrounding dust and H_2 by an order of magnitude. The corresponding *increase* of G (and thus αG) in the models of the aforementioned authors would thus increase their N_{HI} (see e.g. equation 40 and figure 9 in Sternberg et al. 2014) by a factor of a few. This behaviour is thus in general accordance with the interpretation presented here and would bring their upper limits for N_{HI} closer to the values reported here.

⁸ In order to calculate the average visual extinction in a point, one must not take the average $\langle A_{V,i} \rangle$ over different directions i , but must take the logarithm of $\langle \exp(-\gamma A_{V,i}) \rangle$, as the latter describes the amount of incident radiation. The latter averaging puts more emphasis on the low- A_V directions.

5.2 The observational perspective

As observational works on Galactic (e.g. Savage et al. 1977; Kavars et al. 2003, 2005; Klaassen et al. 2005; Gillmon et al. 2006; Krčo et al. 2008; Barriault et al. 2010; Krčo & Goldsmith 2010; Lee et al. 2012, 2015; Stanimirović et al. 2014; Burkhart et al. 2015; Imara & Burkhart 2016) and extragalactic scales (e.g. Wong & Blitz 2002; Browning et al. 2003; Blitz & Rosolowsky 2004, 2006; Bigiel et al. 2008; Wong et al. 2009) tend to find upper limits of N_{HI} around 10^{21} cm^{-2} (equivalent to $8 M_\odot \text{ pc}^{-2}$), it could be argued that the high HI column densities in MCs and the associated underestimation of HI by a factor of 3-10 suggested in this work are rather exceptional. Given the various reasons discussed in this work, however, we argue that the underestimation is indeed rather common. In addition, carefully investigating the observational literature we find further evidence that an upper N_{HI} threshold of 10^{21} cm^{-2} could be artificial:

- Some of the aforementioned HI measurements are emission observations, and for some of them the contribution of the cold HI might be omitted, e.g. Lee et al. (2012) report two absorption features in their HI spectra of the Perseus molecular clouds, which they do not consider in their N_{HI} calculations. Furthermore, other highly-resolved HI emission observations indeed find HI column densities well above 10^{21} cm^{-2} (Fukui et al. 2014, 2015; Motte et al. 2014; Bihr et al. 2015; Okamoto et al. 2017; Syed et al. 2020; Wang et al. 2020b).
- Observations in emission often assume optically thin emission. However, as large parts of MCs have optical depths well above 1 (Fig. 9), optical depth corrections are crucial to infer the correct HI column densities. This is in line with observations of W43 by Bihr et al. (2015), who find an increase in HI by a factor of ~ 2 compared to the optically thin assumption (Motte et al. 2014). Similar correction factors were found for off-Galactic plane HI gas (Fukui et al. 2015) and the Perseus molecular cloud (Okamoto et al. 2017), although for the latter Lee et al. (2012, 2015) argue for a correction of $\sim 20\%$ only. For the THOR survey Wang et al. (2020a) determined the correction factor to $\sim 31\%$. All these correction factors are lower limit as optical depth estimates have an upper limit set by the observational noise (Bihr et al. 2015, and our Eq. 11).
- Finally, extragalactic observations typically have spatial reso-

lutions of a few 100 pc. Hence, they average over clouds and the surrounding diffuse ISM, which can lower the maximum value of N_{HI} significantly. When calculating the total HI column density (now including again HI with $T > 100$ K) for our simulations using only 4 times 4 pixels with a side length of 31.5 pc to cover the entire zoom-in region around the MCs, the maximum value of N_{HI} indeed decreases by about one order of magnitude to $\sim 10^{21} \text{ cm}^{-2}$ (black dots in the top panel of Fig. 1).

To summarize, we suggest that (i) HI column densities well beyond 10^{21} cm^{-2} ($\sim 8 M_{\odot} \text{ pc}^{-2}$) are significantly more common in MCs than thought (Fig. 5) and (ii) also the entire mass of cold HI gas in clouds could be a factor of a few higher ($\gtrsim 3$) than thought (Fig. 11). Vice versa, we argue that (iii) 1-dimensional PDR models might underestimate the amount of cold HI in a typical HI-H₂ transition layer as those are in general not plane-parallel or spherically symmetric objects and (iv) HI observations might underestimate the HI content in MCs by a factor of a few due to the various systematic observational biases discussed in this work.

6 CONCLUSIONS

In this work we present the first fully self-consistent synthetic HI 21 cm observations including self-absorption (HISA) of MCs simulated within the SILCC-Zoom project. The synthetic observations are based on 3D MHD simulations including a non-equilibrium HI-H₂ chemistry, detailed radiative transfer calculations, and realistic observational effects like noise and a limited spectral and spatial resolution adapted to actual observations. In addition, we analyse in detail the actual content of cold HI in the simulated clouds and compare it with the results obtained from the synthetic HISA observations. We summarize our main results in the following.

- We show that HISA observations typically tend to underestimate column densities of cold HI, N_{HI} , and the total cold HI mass in molecular clouds by a factor of 3 – 10. This effect is particular pronounced towards high-column density regions, which frequently reach column densities up to $\gtrsim 10^{22} \text{ cm}^{-2}$. It occurs for MCs under various conditions, e.g. with and without dynamically important magnetic fields.

- We show that the underestimation of N_{HI} in HISA observations can be attributed to the following two effects. (i) The large temperature variations of cold HI (~ 10 K up to 100 K) make a reliable determination of T_{HISA} not possible. This leads to the fact that the real T_{HISA} and thus N_{HI} are underestimated and that velocity channels have to be omitted for the calculation of N_{HI} . This effect occurs when a fixed T_{HISA} is used for the entire map but also when each pixel is given an individual value of T_{HISA} . (ii) Observational noise and the emission of warm HI in the foreground either reduce the inferred optical depth or – as before – cause individual velocity channels to be omitted for the calculation of N_{HI} . This effect is particularly pronounced in regions of high optical depth. In combination, both effects (i + ii) can lead to an artificial upper limit in observation of $N_{\text{HI,obs}}$ around 10^{21} cm^{-2} .

- We suggest a method to correct for the aforementioned omission of high optical depth channels. This correction reduces underestimation of the HI mass budget by a factor of 1.5 – 2.

- We find that clouds typically have HI optical depths around 1 – 10. This implies that the optically thin HI assumption is usually not suitable and that optical depth corrections are essential when calculating N_{HI} from HI observations.

- We show that the high HI column densities ($\gtrsim 10^{22} \text{ cm}^{-2}$) can

(in parts) be attributed to the occurrence of up to 10 individual HI-H₂ transitions along the LOS. However, also for a single HI-H₂ transition, N_{HI} frequently exceeds a value of 10^{21} cm^{-2} , thus challenging 1-dimensional, semi-analytical models. This can be attributed to non-equilibrium chemistry effects, which are included in our models, and to the fact that HI-H₂ transitions usually do not have a 1-dimensional geometry, i.e. to the fractal structure of MCs.

- We demonstrate that N_{HI} -PDFs obtained from HISA observations should be considered with great caution both concerning the position of the peak and the width. Due to the underestimation of HI, the observed PDFs appear to lack the high- N_{HI} end, which in reality seems to be characterised by a power-law.

- Finally, we show that the cold HI gas in MCs is moderately supersonic with Mach numbers of up to a few. The corresponding non-thermal velocity dispersion can be determined via HISA observations with an accuracy of a factor of ~ 2 .

To summarize, our result indicate that measuring the HI content in MCs via HISA observations is a challenging task and that the amount of cold HI in MCs could be a factor of 3 – 10 higher than previously thought.

ACKNOWLEDGEMENTS

DS likes to thank H. Dénes for helpful discussions. DS and SW acknowledge support of the Bonn-Cologne Graduate School, which is funded through the German Excellence Initiative as well as funding by the Deutsche Forschungsgemeinschaft (DFG) via the Collaborative Research Center SFB 956 “Conditions and Impact of Star Formation” (subprojects C5 and C6). SW acknowledges support via the ERC starting grant No. 679852 “RADFEEDBACK”. HB and JDS acknowledge support from the European Research Council under the Horizon 2020 Framework Program via the ERC Consolidator Grant CSF-648505. HB and JS acknowledge support from the DFG in the Collaborative Research Center SFB 881 - Project-ID 138713538 - “The Milky Way System” (subproject B1). PG acknowledges funding from the European Research Council under ERC-CoG grant CRAGSMAN-646955 and the ERC Synergy Grant ECOGAL (grant 855130). RW acknowledges support by project 19-15008S of the Czech Science Foundation and by the institutional project RVO:67985815. The FLASH code used in this work was partly developed by the Flash Center for Computational Science at the University of Chicago. The authors acknowledge the Leibniz-Rechenzentrum Garching for providing computing time on SuperMUC via the project “pr94du” as well as the Gauss Centre for Supercomputing e.V. (www.gauss-centre.eu).

DATA AVAILABILITY

The data underlying this article can be shared for selected scientific purposes after request to the corresponding author.

REFERENCES

- Acreman D. M., Douglas K. A., Dobbs C. L., Brunt C. M., 2010, *MNRAS*, **406**, 1460
- Acreman D. M., Dobbs C. L., Brunt C. M., Douglas K. A., 2012, *MNRAS*, **422**, 241
- Auddy S., Basu S., Kudoh T., 2018, *MNRAS*, **474**, 400
- Barriault L., et al., 2010, *MNRAS*, **406**, 2713

- Beck R., Wiebeinski R., 2013, *Magnetic Fields in Galaxies*. p. 641, doi:10.1007/978-94-007-5612-0_13
- Bellomi E., Godard B., Hennebelle P., Valdivia V., Pineau des Forêts G., Lesaffre P., Pérault M., 2020, *A&A*, **643**, A36
- Beuther H., et al., 2020, *A&A*, **638**, A44
- Bialy S., Sternberg A., 2016, *ApJ*, **822**, 83
- Bialy S., Bihl S., Beuther H., Henning T., Sternberg A., 2017a, *ApJ*, **835**, 126
- Bialy S., Burkhart B., Sternberg A., 2017b, *ApJ*, **843**, 92
- Bigiel F., Leroy A., Walter F., Brinks E., de Blok W. J. G., Madore B., Thornley M. D., 2008, *AJ*, **136**, 2846
- Bihl S., et al., 2015, *A&A*, **580**, A112
- Blitz L., Rosolowsky E., 2004, *ApJ*, **612**, L29
- Blitz L., Rosolowsky E., 2006, *ApJ*, **650**, 933
- Bolatto A. D., Wolfire M., Leroy A. K., 2013, *ARA&A*, **51**, 207
- Browning M. K., Tumlinson J., Shull J. M., 2003, *ApJ*, **582**, 810
- Burkhart B., Lazarian A., 2012, *ApJ*, **755**, L19
- Burkhart B., Lee M.-Y., Murray C. E., Stanimirović S., 2015, *ApJ*, **811**, L28
- Clark P. C., Glover S. C. O., Klessen R. S., 2012a, *MNRAS*, **420**, 745
- Clark P. C., Glover S. C. O., Klessen R. S., Bonnell I. A., 2012b, *MNRAS*, **424**, 2599
- Clark P. C., Glover S. C. O., Ragan S. E., Duarte-Cabral A., 2019, *MNRAS*, **486**, 4622
- Clarke S. D., Whitworth A. P., Spowage R. L., Duarte-Cabral A., Suri S. T., Jaffa S. E., Walch S., Clark P. C., 2018, *MNRAS*, **479**, 1722
- Dénes H., McClure-Griffiths N. M., Dickey J. M., Dawson J. R., Murray C. E., 2018, *MNRAS*, **479**, 1465
- Dobbs C. L., et al., 2014, in Beuther H., Klessen R. S., Dullemond C. P., Henning T., eds, *Protostars and Planets VI*. p. 3 (arXiv:1312.3223), doi:10.2458/azu_uapress_9780816531240-ch001
- Douglas K. A., Acreman D. M., Dobbs C. L., Brunt C. M., 2010, *MNRAS*, **407**, 405
- Draine B. T., 1978, *ApJS*, **36**, 595
- Dubey A., et al., 2008, in Pogorelov N. V., Audit E., Zank G. P., eds, *Astronomical Society of the Pacific Conference Series Vol. 385, Numerical Modeling of Space Plasma Flows*. p. 145
- Dullemond C. P., Juhasz A., Pohl A., Sereshti F., Shetty R., Peters T., Commercon B., Flock M., 2012, *RADMC-3D: A multi-purpose radiative transfer tool* (ascl:1202.015)
- Feldt C., 1993, *A&A*, **276**, 531
- Field G. B., 1958, *Proceedings of the IRE*, **46**, 240
- Field G. B., 1959, *ApJ*, **129**, 551
- Fryxell B., et al., 2000, *ApJS*, **131**, 273
- Fukui Y., et al., 2014, *ApJ*, **796**, 59
- Fukui Y., Torii K., Onishi T., Yamamoto H., Okamoto R., Hayakawa T., Tachihara K., Sano H., 2015, *ApJ*, **798**, 6
- Fukui Y., Hayakawa T., Inoue T., Torii K., Okamoto R., Tachihara K., Onishi T., Hayashi K., 2018, *ApJ*, **860**, 33
- Gatto A., et al., 2017, *MNRAS*, **466**, 1903
- Gibson S. J., Taylor A. R., Higgs L. A., Dewdney P. E., 2000, *ApJ*, **540**, 851
- Gibson S. J., Taylor A. R., Higgs L. A., Brunt C. M., Dewdney P. E., 2005, *ApJ*, **626**, 195
- Gillmon K., Shull J. M., Tumlinson J., Danforth C., 2006, *ApJ*, **636**, 891
- Girichidis P., Konstantin L., Whitworth A. P., Klessen R. S., 2014, *ApJ*, **781**, 91
- Girichidis P., et al., 2016, *MNRAS*, **456**, 3432
- Glover S. C. O., Clark P. C., 2012, *MNRAS*, **421**, 116
- Glover S. C. O., Mac Low M.-M., 2007a, *ApJS*, **169**, 239
- Glover S. C. O., Mac Low M.-M., 2007b, *ApJ*, **659**, 1317
- Glover S. C. O., Federrath C., Mac Low M.-M., Klessen R. S., 2010, *MNRAS*, **404**, 2
- Gnedin N. Y., Tassis K., Kravtsov A. V., 2009, *ApJ*, **697**, 55
- Goldsmith P. F., Li D., 2005, *ApJ*, **622**, 938
- Goodman A. A., Heiles C., 1994, *ApJ*, **424**, 208
- Gould R. J., 1994, *ApJ*, **423**, 522
- Habing H. J., 1968, *Bull. Astron. Inst. Netherlands*, **19**, 421
- Haid S., Walch S., Seifried D., Wünsch R., Dinnbier F., Naab T., 2019, *MNRAS*, **482**, 4062
- Heeschen D. S., 1954, *AJ*, **59**, 324
- Heeschen D. S., 1955, *ApJ*, **121**, 569
- Heiner J. S., Vázquez-Semadeni E., Ballesteros-Paredes J., 2015, *MNRAS*, **452**, 1353
- Hennebelle P., Audit E., Miville-Deschênes M. A., 2007, *A&A*, **465**, 445
- Imara N., Burkhart B., 2016, *ApJ*, **829**, 102
- Joshi P. R., Walch S., Seifried D., Glover S. C. O., Clarke S. D., Weis M., 2019, *MNRAS*, **484**, 1735
- Kainulainen J., Beuther H., Henning T., Plume R., 2009, *A&A*, **508**, L35
- Kalberla P. M. W., Burton W. B., Hartmann D., Arnal E. M., Bajaja E., Morras R., Pöppel W. G. L., 2005, *A&A*, **440**, 775
- Kavars D. W., Dickey J. M., McClure-Griffiths N. M., Gaensler B. M., Green A. J., 2003, *ApJ*, **598**, 1048
- Kavars D. W., Dickey J. M., McClure-Griffiths N. M., Gaensler B. M., Green A. J., 2005, *ApJ*, **626**, 887
- Kim C.-G., Ostriker E. C., Kim W.-T., 2014, *ApJ*, **786**, 64
- Klaassen P. D., Plume R., Gibson S. J., Taylor A. R., Brunt C. M., 2005, *ApJ*, **631**, 1001
- Knapp G. R., 1974, *AJ*, **79**, 527
- Kritsuk A. G., Norman M. L., Wagner R., 2011, *ApJ*, **727**, L20
- Krumholz M. R., McKee C. F., Tumlinson J., 2008, *ApJ*, **689**, 865
- Krumholz M. R., McKee C. F., Tumlinson J., 2009, *ApJ*, **693**, 216
- Krčo M., Goldsmith P. F., 2010, *ApJ*, **724**, 1402
- Krčo M., Goldsmith P. F., Brown R. L., Li D., 2008, *ApJ*, **689**, 276
- Lee M.-Y., et al., 2012, *ApJ*, **748**, 75
- Lee M.-Y., Stanimirović S., Murray C. E., Heiles C., Miller J., 2015, *ApJ*, **809**, 56
- Li D., Goldsmith P. F., 2003, *ApJ*, **585**, 823
- Liszt H., 2001, *A&A*, **371**, 698
- Mac Low M.-M., Glover S. C. O., 2012, *ApJ*, **746**, 135
- Mackey J., Walch S., Seifried D., Glover S. C. O., Wünsch R., Aharonian F., 2019, *MNRAS*, **486**, 1094
- McClure-Griffiths N. M., Dickey J. M., Gaensler B. M., Green A. J., Haverkorn M., 2006, *ApJ*, **652**, 1339
- McKee C. F., Krumholz M. R., 2010, *ApJ*, **709**, 308
- Montgomery A. S., Bates B., Davies R. D., 1995, *MNRAS*, **273**, 449
- Motte F., et al., 2014, *A&A*, **571**, A32
- Murray C. E., et al., 2015, *ApJ*, **804**, 89
- Murray C. E., Stanimirović S., Kim C.-G., Ostriker E. C., Lindner R. R., Heiles C., Dickey J. M., Babler B., 2017, *ApJ*, **837**, 55
- Murray C. E., Peek J. E. G., Lee M.-Y., Stanimirović S., 2018, *ApJ*, **862**, 131
- Nelson R. P., Langer W. D., 1999, *ApJ*, **524**, 923
- Nickerson S., Teyssier R., Rosdahl J., 2019, *MNRAS*, **484**, 1238
- Okamoto R., Yamamoto H., Tachihara K., Hayakawa T., Hayashi K., Fukui Y., 2017, *ApJ*, **838**, 132
- Rachford B. L., et al., 2009, *ApJS*, **180**, 125
- Rebolledo D., et al., 2017, *MNRAS*, **472**, 1685
- Riegel K. W., Crutcher R. M., 1972, *A&A*, **18**, 55
- Röllig M., et al., 2007, *A&A*, **467**, 187
- Savage B. D., Bohlin R. C., Drake J. F., Budich W., 1977, *ApJ*, **216**, 291
- Schneider N., et al., 2015, *A&A*, **575**, A79
- Schruba A., et al., 2011, *AJ*, **142**, 37
- Seifried D., et al., 2017, *MNRAS*, **472**, 4797
- Seifried D., Walch S., Haid S., Girichidis P., Naab T., 2018, *ApJ*, **855**, 81
- Seifried D., Walch S., Reissl S., Ibáñez-Mejía J. C., 2019, *MNRAS*, **482**, 2697
- Seifried D., Haid S., Walch S., Borchert E. M. A., Bisbas T. G., 2020a, *MNRAS*, **492**, 1465
- Seifried D., Walch S., Weis M., Reissl S., Soler J. D., Klessen R. S., Joshi P. R., 2020b, *MNRAS*, **497**, 4196
- Smith R. J., et al., 2020, *MNRAS*, **492**, 1594
- Soler J. D., 2019, *A&A*, **629**, A96
- Soler J. D., et al., 2019, *A&A*, **622**, A166
- Stanimirović S., Murray C. E., Lee M.-Y., Heiles C., Miller J., 2014, *ApJ*, **793**, 132
- Sternberg A., 1988, *ApJ*, **332**, 400
- Sternberg A., Le Petit F., Roueff E., Le Bourlot J., 2014, *ApJ*, **790**, 10
- Syed J., et al., 2020, *A&A*, **642**, A68
- Valdivia V., Hennebelle P., Gérin M., Lesaffre P., 2016, *A&A*, **587**, A76

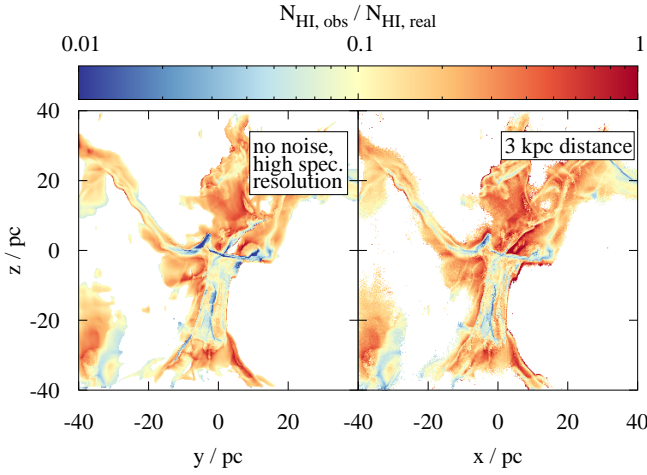


Figure A1. Map of the ratio of the observed and actual HI column density for the same snapshot as in Fig. 4, now for the case of no noise and a high spectral resolution (left) and an assumed distance of 3 kpc including observational effects like noise (right) inferred from the HISA observation assuming $T_{\text{HISA}} = 40$ K. The poor match is found also for the ideal observations (left) supporting the conclusion that strong temperature variation are (in parts) the cause for it.

Veltchev T. V., Girichidis P., Donkov S., Schneider N., Stanchev O., Marinkova L., Seifried D., Klessen R. S., 2019, *MNRAS*, **489**, 788
 Walch S., et al., 2015, *MNRAS*, **454**, 238
 Wang Y., et al., 2020a, *A&A*, **634**, A83
 Wang Y., et al., 2020b, *A&A*, **634**, A139
 Welty D. E., Xue R., Wong T., 2012, *ApJ*, **745**, 173
 Wilson T. L., Rohlfs K., Hüttemeister S., 2013, *Tools of Radio Astronomy*, doi:10.1007/978-3-642-39950-3.
 Wolfire M. G., Hollenbach D., McKee C. F., 2010, *ApJ*, **716**, 1191
 Wong T., Blitz L., 2002, *ApJ*, **569**, 157
 Wong T., et al., 2009, *ApJ*, **696**, 370
 Wouthuysen S. A., 1952, *AJ*, **57**, 31
 Wünsch R., Walch S., Dinnbier F., Whitworth A., 2018, *MNRAS*,
 van Dishoeck E. F., Black J. H., 1986, *ApJS*, **62**, 109
 van der Werf P. P., Goss W. M., Vanden Bout P. A., 1988, *A&A*, **201**, 311

APPENDIX A: SUPPLEMENTARY FIGURES

In the left panel of Fig. A1 we show ratio of $N_{\text{HI,obs}}$ to $N_{\text{HI,real}}$ for MC1-HD at 2 Myr, where $N_{\text{HI,obs}}$ is calculated from the noiseless, high-spectral resolution (200 m s^{-1}) maps obtained directly from RADMC-3D using $T_{\text{HISA}} = 40$ K. We find a comparable poor match as for the case when observational effects are included. In the right panel we show the results obtained assuming a distance of 3 kpc (again including observational effects). Little differences are found compared to a distance of 150 pc (compare with the bottom middle panel of Fig. 4). This result holds also for the other snapshots considered in this work.

In Fig. A2 we show the inferred HI column density for MC1-HD at 2 Myr now including the correction in optically thick regions. The results are discussed in Section 3.3.1.

In Fig. A3 we show the effect of post-processing the chemical state of one of our simulation, i.e. pushing it towards a chemical equilibrium state. This is done exemplarily for MC1-HD taking two snapshots at $t_{\text{evol}} = 2$ and 3 Myr considered in this work. We stop the magneto-hydrodynamical evolution at these time, i.e. freeze the total density, velocity, etc., and only evolve the chemistry for additional

100 Myr. The chemical post-processing time (measured from t_{evol} onwards) is denoted as t_{chem} . The HI content quickly drops to 40 – 50% of the actual (non-equilibrium) HI content (at $t_{\text{chem}} = 0$), which indicates that equilibrium models generally underestimate the amount of HI in MCs.

In Fig. A4 we show the $\log(n_{\text{HI}})$ -profile for 5 selected pixels for MC1 at 2 Myr along the x -direction used for the analysis in Section 4.2. The profiles show a large variability concerning the number of peaks, their widths and positions. Some of the peaks are discarded as they do not have either the required minimum prominence or the minimum peak height.

APPENDIX B: AN APPROXIMATION FOR THE OPTICAL DEPTH

In order to estimate the optical depth of the HI gas in our simulations, we repeat one radiative transfer calculation for MC1-HD, however, now setting the background temperature to 0 K. Hence, the observed emission purely stems from the HI gas in the zoom-in region.

As noted in Eq. 7, but now written down for a single velocity channel, the HI column density is given by

$$dN_{\text{HI}} = 1.8224 \times 10^{18} \text{ cm}^{-2} \frac{T_s}{1 \text{ K}} \tau(\nu) \frac{d\nu}{1 \text{ km s}^{-1}}. \quad (\text{B1})$$

Next, we consider the expression

$$T_{\text{rad}} = \frac{h\nu_{\text{HI}}}{k_B} \left(f(T_s) - f(T_{\text{bg}}) \right) (1 - e^{-\tau}), \quad (\text{B2})$$

for the observed radiation temperature T_{rad} . Here, T_{bg} is the background temperature, h is the Planck constant, k_B the Boltzmann constant, $\nu_{\text{HI}} = 1420$ MHz the frequency of the HI 21-cm line, and

$$f(T) = \frac{1}{\exp\left(\frac{h\nu_{\text{HI}}}{k_B T}\right) - 1}. \quad (\text{B3})$$

Considering that $h\nu_{\text{HI}}/k_B = 0.068 \text{ K} \ll T_s$ and $f(T_{\text{bg}}) \ll f(T_s)$, and inserting Eq. B2 in Eq. B1 yields

$$dN_{\text{HI}} \simeq 1.8224 \times 10^{18} \text{ cm}^{-2} \frac{\tau}{1 - e^{-\tau}} \frac{T_{\text{rad}}}{1 \text{ K}} \frac{d\nu}{1 \text{ km s}^{-1}}. \quad (\text{B4})$$

We now integrate over all velocity channels using a definition of a T_{rad} -weighted, channel-averaged approximation of the optical depth

$$N_{\text{HI}} = 1.8224 \times 10^{18} \text{ cm}^{-2} \langle \tau \rangle \int \frac{T_{\text{rad}}}{1 \text{ K}} \frac{d\nu}{1 \text{ km s}^{-1}}. \quad (\text{B5})$$

Here, we have defined

$$\langle \tau \rangle = \frac{\int \frac{\tau}{1 - e^{-\tau}} T_{\text{rad}} d\nu}{\int T_{\text{rad}} d\nu}. \quad (\text{B6})$$

The interpretation of $\langle \tau \rangle$ as an approximation for a T_{rad} -weighted, channel-averaged optical depth can be understood, when considering the fact that $\frac{\tau}{1 - e^{-\tau}} \rightarrow \tau$ with $\tau \rightarrow \infty$. For $\tau = 1$, the expression $\frac{\tau}{1 - e^{-\tau}}$ is only $\sim 50\%$ larger than τ , for $\tau = 2$ only $\sim 15\%$. For optically thin regions ($\tau < 1$), the approximation is not applicable. However, as in Section 3.3 we are mainly interested in high optical depth regions, we consider our definition of $\langle \tau \rangle$ as a reasonable approximation for the typical optical depth of HI in our simulations.

Next, using the integrated intensity from the radiative transfer calculations without any background radiation field and the real HI column density from the simulation data, $N_{\text{HI,real}}$, we can now calculate $\langle \tau \rangle$ via

$$\langle \tau \rangle = \frac{N_{\text{HI,real}}}{1.8224 \times 10^{18} \text{ cm}^{-2} \int \frac{T_{\text{rad}}}{1 \text{ K}} \frac{d\nu}{1 \text{ km s}^{-1}}}, \quad (\text{B7})$$

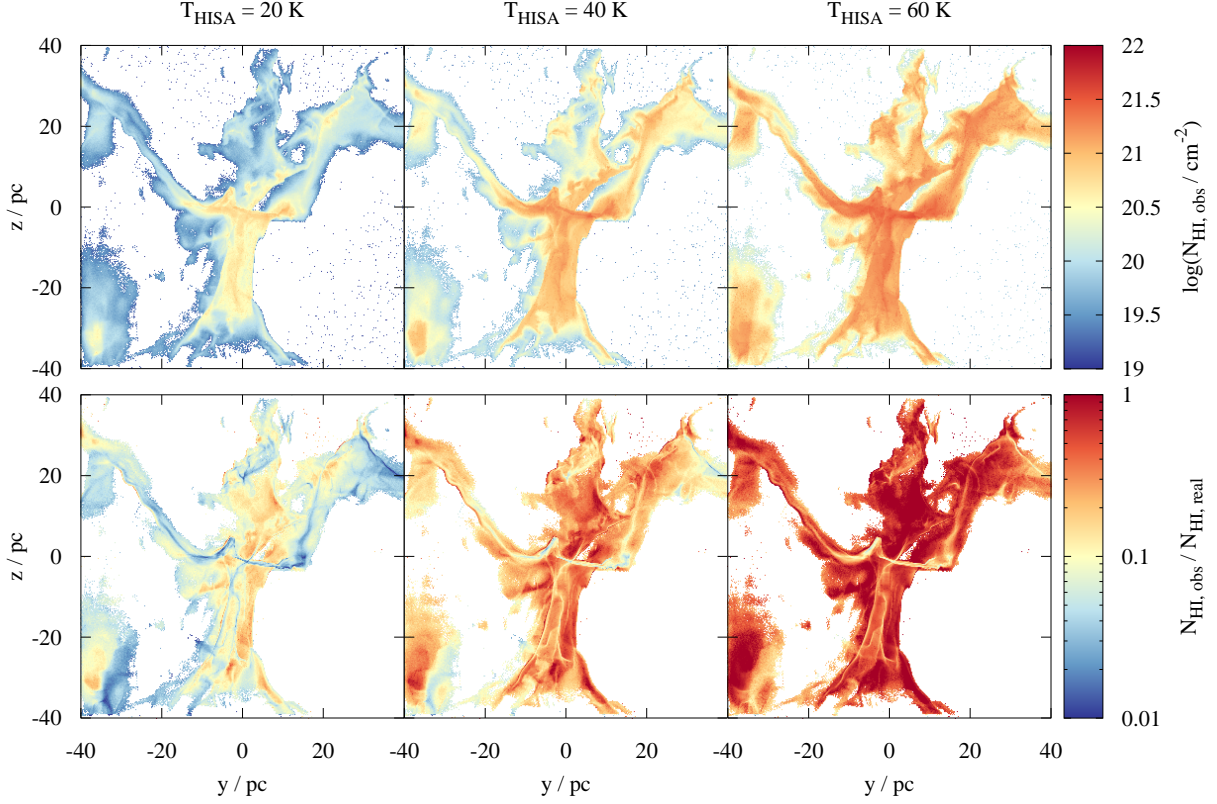


Figure A2. Same as in Fig. 4, but now with the correction in optically thick regions where for channels, where Eq. 6 does not yield any result, we assume an optical depth given by $\tau_{\text{HI,noise}}$ (Eq. 11). Overall, the match in the moderately dense gas is improved, whereas in the most densest parts $N_{\text{HI,real}}$ is still significantly underestimated.

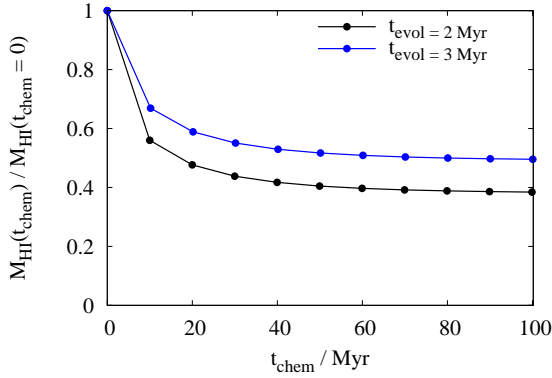


Figure A3. Evolution of the HI content of MC1-HD when post-processing the chemical abundances for a time of t_{chem} relative to the actual (non-equilibrium) HI content (at $t_{\text{chem}} = 0$). Assuming chemical equilibrium would reduce the HI content by a factor of 2 – 2.5.

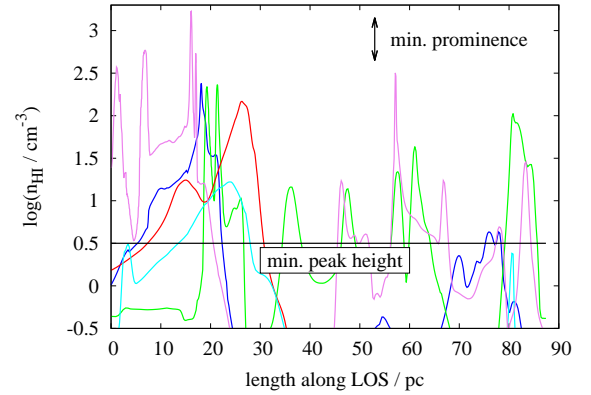


Figure A4. Profiles of $\log(n_{\text{HI}})$ for 5 selected pixels for MC1 at 2 Myr along the x -direction. The profiles show a large variability. In addition we show the minimum prominence and minimum peak value (both in black), which a peak must have to be considered and not discarded.

where the denominator is describing the HI column density obtained from HI emission under the assumption of optically thin emission.

This paper has been typeset from a \LaTeX file prepared by the author.